



TALLINN UNIVERSITY OF TECHNOLOGY  
SCHOOL OF ENGINEERING  
Department's title

**IMPACT OF SULFUR ANNEALING ON THE  
 $\text{Cu}_2\text{ZnSnS}_4$  MONOGRAIN POWDER PROPERTIES  
AND SOLAR CELL PARAMETERS**

**VÄÄVLI AURURÕHU TÖÖTLUSTE MÕJU  $\text{Cu}_2\text{ZnSnS}_4$   
MONOTERAPULBRITE OMADUSTELE JA  
PÄIKESEPATAREI VÄLJUNDPARAMEETRITELE**

MASTER THESIS

Student: Marc Dolcet Sadurni

Student code: 201674KAYM

Supervisor: Dr. Kristi Timmo  
Senior Researcher

Tallinn 2022

(On the reverse side of title page)

## **AUTHOR'S DECLARATION**

Hereby I declare, that I have written this thesis independently.

No academic degree has been applied for based on this material. All works, major viewpoints and data of the other authors used in this thesis have been referenced.

"....." ..... 20.....

Author: .....  
*/signature /*

Thesis is in accordance with terms and requirements

"....." ..... 20....

Supervisor: .....  
*/signature/*

Accepted for defence

"....." .....20... .

Chairman of theses defence commission: .....  
*/name and signature/*

## **Non-exclusive licence for reproduction and publication of a graduation thesis<sup>1</sup>**

I Marc Dolcet Sadurni

1. grant Tallinn University of Technology free licence (non-exclusive licence) for my thesis

“Impact of sulfur annealing on the Cu<sub>2</sub>ZnSnS<sub>4</sub> monograin powder properties and solar cell parameters”,

supervised by Dr. Kristi Timmo,

1.1 to be reproduced for the purposes of preservation and electronic publication of the graduation thesis, incl. to be entered in the digital collection of the library of Tallinn University of Technology until expiry of the term of copyright;

1.2 to be published via the web of Tallinn University of Technology, incl. to be entered in the digital collection of the library of Tallinn University of Technology until expiry of the term of copyright.

2. I am aware that the author also retains the rights specified in clause 1 of the non-exclusive licence.

3. I confirm that granting the non-exclusive licence does not infringe other persons' intellectual property rights, the rights arising from the Personal Data Protection Act or rights arising from other legislation.

---

22.05.2022

---

<sup>1</sup> *The non-exclusive licence is not valid during the validity of access restriction indicated in the student's application for restriction on access to the graduation thesis that has been signed by the school's dean, except in case of the university's right to reproduce the thesis for preservation purposes only. If a graduation thesis is based on the joint creative activity of two or more persons and the co-author(s) has/have not granted, by the set deadline, the student defending his/her graduation thesis consent to reproduce and publish the graduation thesis in compliance with clauses 1.1 and 1.2 of the non-exclusive licence, the non-exclusive license shall not be valid for the period.*

## THESIS TASK

**Student:** Marc Dolcet Sadurni, 201674KAYM

Study programme, KAYM, Materials and Processes of Sustainable Energetics (code and title)

main speciality: Materials of Sustainable Energetics

Supervisor(s): Senior Researcher, Dr. Kristi Timmo, +372 620 3362

(position, name, phone)

Consultants: .....(name, position)

..... (company, phone, e-mail)

**Thesis topic:**

(in English) *Impact of sulfur annealing on the Cu<sub>2</sub>ZnSnS<sub>4</sub> monograin powder properties and solar cell parameters.*

(in Estonian) *Väävli aururõhu töötluste mõju Cu<sub>2</sub>ZnSnS<sub>4</sub> monoterapulbrite omadustele ja päikesepatarei väljundparameetritele*

**Thesis main objectives:**

1. to investigate the influence of post-annealing in sulfur atmosphere on kesterite material Cu<sub>2</sub>ZnSnS<sub>4</sub> properties
2. to find out the optimal conditions for the post-treatment of Cu<sub>2</sub>ZnSnS<sub>4</sub> monograin powders to improve MGL solar cells` performance

**Thesis tasks and time schedule:**

No	Task description	Deadline
1.	Etching and annealing the Cu <sub>2</sub> ZnSnS <sub>4</sub> monograin powders under different regimes. Characterization of the crystals` surfaces and bulk composition of CZTS monograin powders	19.02.2021
2.	Preparation and characterization of solar cells based on CZTS monograin powders	18.06.2021
3.	Writing the thesis report	20.05.2022

**Language:** English **Deadline for submission of thesis:** "23"05 2022 a

**Student:** Marc Dolcet Sadurni ..... ".....".....2022 a  
/signature/

**Supervisor:** Dr. Kristi Timmo ..... ".....".....2022 a  
/signature/

**Consultant:** ..... ".....".....20....a

*/signature/*

**Head of study programme:** Dr. Sergei Bereznev ..... “.....”.....2022 a

*/signature/*

*Terms of thesis closed defence and/or restricted access conditions to be formulated on the reverse side*

## CONTENTS

PREFACE .....	8
List of abbreviations and symbols .....	9
INTRODUCTION.....	10
1. LITERATURE REVIEW .....	12
1.1 Fundamentals of solar cells .....	12
1.1.1 Structure and working principle of semiconductors .....	12
1.1.2 <i>p-n</i> junction formation .....	14
1.1.3 Efficiency limitations in solar cells.....	16
1.2 Solar cell absorber materials - overview .....	18
1.2.1 Kesterite based absorber materials.....	19
1.2.2 Crystal structure .....	19
1.2.3 Phase diagram of CZTS .....	20
1.2.4 Preparation methods of CZTS .....	21
1.3 Post-treatment of CZTS .....	22
1.3.1 Chemical etching.....	22
1.3.2 Thermal treatment .....	23
1.4 Monograin powder technology .....	25
1.4.1 Monograin Powder Growth.....	25
1.4.2 Monograin Layer Solar Cells.....	26
1.5 Summary of the literature review and the aim of the study .....	27
2. METHODOLOGY .....	29
2.1 Post-treatments of asgrown monograins.....	29
2.1.1 Chemical etchings of monograin powder crystals` surfaces.....	29
2.1.2 Post-annealing in different atmospheres.....	29
2.2 Preparation of MGL solar cells.....	31
2.3 Characterization of monograin powders and monograin layer solar cells .....	32
2.3.1 Energy Dispersive X-ray Spectroscopy (EDX) .....	32
2.3.2 Scanning Electron Microscopy (SEM).....	33
2.3.3 Room Temperature Micro-Raman Spectroscopy.....	33
2.3.4 Current-Voltage ( <i>I-V</i> ) Characterization.....	34
2.3.5 Quantum Efficiency (QE) Measurements.....	35
2.3.6 Electron Beam Induced Current (EBIC) measurements.....	35
3. RESULTS AND DISCUSSION.....	36
3.1 Post annealing in sulfur atmosphere.....	36
3.1.1 Morphology of the CZTS monograins after post-annealing in sulfur atmosphere.....	36

3.1.2 Phase composition of $\text{Cu}_2\text{ZnSnS}_4$ monograin powder crystals` surfaces after post-annealing in sulfur atmosphere .....	39
3.1.3 Bulk composition of CZTS monograins after post-annealing in sulfur atmosphere.....	42
3.1.4 Characterization of the monograin layer solar cells .....	45
3.2 Post annealing in sulfur and argon atmosphere.....	48
3.2.1 Elemental composition of CZTS monograin powders post-annealed in sulfur and argon atmosphere .....	50
3.2.2 Morphology of CZTS monograin powders post-annealed in sulfur and argon atmosphere.....	52
3.2.3 Characterization of the MGL solar cells based on CZTS monograin powders annealed in sulfur and argon atmosphere .....	53
SUMMARY.....	56
LIST OF REFERENCES .....	58

## PREFACE

My supervisor and senior researcher Dr Kristi Timmo proposed the topic of the following thesis. This thesis is based on the experimental work carried out in the Laboratory of Photovoltaic Materials at the Department of Materials and Environmental Technology, Tallinn University of Technology (TalTech). This work was supported by the Estonian Research Council project PRG1023, by ERDF project „Center of nanomaterials technologies and research (NAMUR+)” (2020.4.01.16-0123), by the European Union through the European Regional Development Fund, Project TK141 and by European Union’s H2020 research and innovation programme under Grant Agreement No. 952982.

First of all, I would like to express my deepest gratitude to my supervisor, senior researcher Dr. Kristi Timmo for her guidance, support, aid and tons of hours invested on me during this thesis. I would like to thank senior researcher Dr. Maris Pilvet for her patience while teaching me the art of solar cell preparation. I must thank Xiaofeng Li not only for his help during this thesis through many valuable discussions but also during this whole master program. He’s become such an excellent roommate and a true friend of mine. Thanks to the head of laboratory, Dr. Marit Kauk-Kuusik, Dr. Reelika Kaupmees, Dr. Jaan Raudoja, Dr. Valdek Mikli, Dr. Olga Volobujeva and also the Catalonia Institute for Energy Research (IREC) for their assistance throughout the experimental work of this thesis. I am deeply indebted to Dr. Sergei Bereznev not only for opening the doors of TalTech and to encourage me to start investigating from the very beginning but also for all his dedication and genuine care for us during these two years. Finally, thanks to my family and friends from Catalonia and also the ones I made in Estonia, you were all my closest and strongest support during this period.

In this thesis,  $\text{Cu}_2\text{ZnSnS}_4$  (CZTS) monograin powder absorber materials were synthesized by the molten salt synthesis-growth method. The aim of this study was to investigate the effect of annealing of as-grown CZTS monograin powder crystals at high temperatures (550-850 °C) in a sulfur-containing atmosphere (100-2050 Torr) on the monograin layer solar cells parameters. Optimal conditions for post-annealing to adjust the absorber material composition and to improve MGL solar cells` performance were found to be annealing in sealed ampoules at 850 °C in sulfur atmosphere of 2050 Torr for 1 hour. The highest conversion efficiency 8.42% was achieved under these conditions.

Key Words:  $\text{Cu}_2\text{ZnSnS}_4$ , kesterite, thermal treatment, monograin layer solar cells, master thesis

## List of abbreviations and symbols

PV - Photovoltaic  
LCOE - global weighted-average levelized cost  
CZTS - Copper-Zinc-Tin-Sulfide  
CZTSe - Copper-Zinc-Tin-Selenide  
CZTSSe- Copper-Zinc-Tin-Sulfoselenide  
CIGS - Copper Indium Gallium Selenide  
MGP – Monograin powder  
MGL – Monograin layer solar cell  
STC - Standard test conditions  
SQ - Shockley-Queisser limit  
CVD - chemical vapor deposition  
KCN – Potassium cyanide  
KOH – Potassium hydroxide  
 $E_v$  – Valence band  
 $E_c$  – Conduction band  
 $E_g$  – Band gap  
KI- Potassium iodide  
RT – Room temperature  
CBD – Chemical bath deposition  
DI-H<sub>2</sub>O - Deionized water  
EDX - Energy dispersive x-ray spectroscopy  
SEM - Scanning electron microscopy  
SE – Secondary electrons  
BSE - Back scattered electrons  
QE – Quantum efficiency  
EQE- External quantum efficiency  
IQE - Internal quantum efficiency

# INTRODUCTION

The 2030 climate and energy framework targets to cut at least 40% in greenhouse gas emissions (from 1990 levels) and to achieve at least 32% share for renewable energy in energy consumption [1].

Energy demand is rapidly increasing and renewable energy resources are estimated to reach 60 TW and a 40% of the total share by 2050. It is estimated that renewable energies like photovoltaics will experience an average annual generation growth of 24% between 2020 and 2030 [2].

The major issue photovoltaic (PV) energy has to solve is its high cost production. Impressive progress has been made over the last decade and the trend shows a remarkable cost reduction. For newly commissioned utility-scale projects, the global weighted-average levelized cost (LCOE) has decreased 85 % from 2010 to 2020. Just in 2020 LCOE has fallen 7% [3].

One way of reducing costs of solar cells passes through substituting scarce and toxic materials for more abundant and therefore cheaper materials. The major challenges that future solar cells have to overcome are their efficiency and their durability.

Kesterite materials such as  $\text{Cu}_2\text{ZnSnS}_4$  (Copper-Zinc-Tin-Sulfide),  $\text{Cu}_2\text{ZnSnSe}_4$  (Copper-Zinc-Tin-Selenide) and their solid solutions  $\text{Cu}_2\text{ZnSn}(\text{S},\text{Se})_4$  (Copper-Zinc-Tin-Sulfoselenide) are currently being widely investigated. They have drawn considerable attention due to the necessity to replace expensive and rare Indium and Gallium in Copper Indium Gallium Selenide (CIGS) solar cells with more abundant materials like Zinc and Tin. Although the efficiency of kesterites is still far from CIGS solar cells, the trending is positive and the records in efficiency of kesterites are already  $\sim 13\%$  [4][5].

There are different reasons why kesterites have not been commercialized yet. The phase purity, electronic and optical properties of the absorber layer and interface quality are depending on the preparation technology and are critical as they directly affect the efficiency of  $\text{Cu}_2\text{ZnSn}(\text{S},\text{Se})_4$  solar cells [6]. The quaternary phase  $\text{Cu}_2\text{ZnSnS}_4$  can only be produced in certain conditions and due to that, secondary ( $\text{CuS}$ ,  $\text{ZnS}$ ,  $\text{SnS}$ ,  $\text{Cu}_2\text{S}$ ,  $\text{SnS}_2$ ) and ternary ( $\text{Cu}_2\text{SnS}_3$ ) phases are usually present. Non-desired phases can be removed by different chemical etchings. Lattice defects also affect the performance of the device, playing a big role to the recombination of electron-hole pairs. In order to improve the interface quality different thermal treatments can be carried out [7].

In this work, the high-quality  $\text{Cu}_2\text{ZnSnS}_4$  monograin powder absorber materials are synthesized by molten salt method. Due to the nature of the monograin powder technology, the formation of undesired surface layer on the bulk crystals of the main compound is inevitable. The retained precipitations at the interface of the  $p$ - $n$  junction without some special post-growth treatments, degrade the performance of CZTS MGP based solar cells. Therefore, the development of an effective post-treatment to the monograin powder crystals before the buffer layer deposition is essential and significant. The objective of this research is to study the effect of post-treatment regime (annealing of as-grown powder crystals at high temperatures in a sulfur-containing atmosphere before the deposition of CdS) on the surface and bulk composition of CZTS MGP crystals and MGL solar cell parameters.

# 1. LITERATURE REVIEW

## 1.1 Fundamentals of solar cells

Photovoltaic solar energy (PV) is a type of sustainable and renewable source of energy capable of producing electricity directly from the sunlight. Solar cells are the devices used to obtain energy from the sun radiation through the mechanism called photovoltaic effect. This effect was first reported by Alexandre Edmond Becquerel in 1839 by exposing silver and platinum electrodes to the sunlight. In 1877, Adams and Richard Day developed a device made of selenium achieving an efficiency of approximately 0.5 % but it was Charles Fritts, doubling this efficiency, that one year later created the first solar cell by using a selenium wafer placed between two metal thin layers [8].

The next major advance came in 1954 when Bell Laboratories developed the first silicon solar cell with an efficiency of 6% [9].

### 1.1.1 Structure and working principle of semiconductors

As mentioned before, semiconductor materials are used to absorb light in solar cells. The main reason to use them is their capacity to change their conductivity by adding small amounts of impurities to the semiconductor material.

Semiconductors have a specific bond structure that determines their properties. Atoms in a semiconductor material are bounded in a regular and periodic structure called crystal lattice. In this arrangement, each atom is surrounded by 8 electrons forming covalent bonds. The number of protons in the nucleus is the same as the electrons surrounding it so the total charge is neutral.

Electrons in covalent bonds cannot move freely and only at elevated temperatures they can gain enough energy to move in the crystal lattice and in consequence, participate in conduction to create a current. When an electron has enough energy to move in the crystal lattice it leaves a space behind and the covalent bond can move from one electron to another. This space is called a hole and it can be seen as an electron with a positive charge.

The band diagram of a semiconductor shows the energy necessary to excite an electron from the valence band ( $E_v$ ) to the conduction band ( $E_c$ ) and this energy between these two bands is commonly called band gap ( $E_g$ ). Or in other words, the energy difference between free electrons and bound electrons (see Figure 1.1).

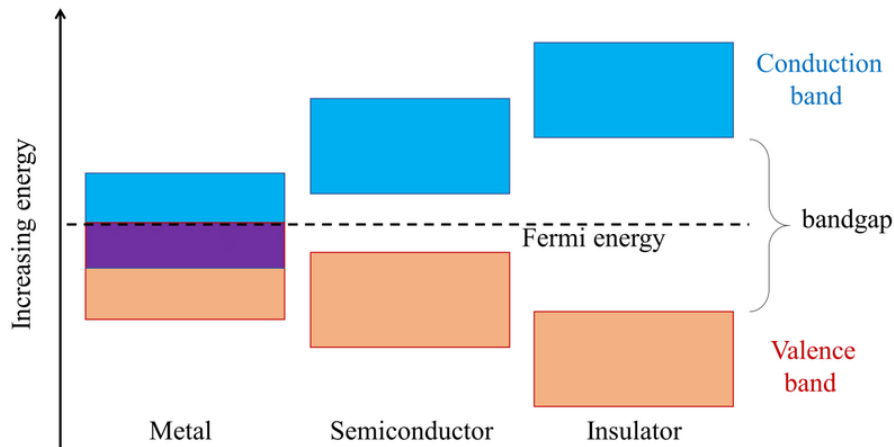


Figure 1.1 Band diagram of a metal (left), a semiconductor (middle) and an insulator (right) [10]

The current flow in a semiconductor can be produced by the motion of all the free electrons in the conduction band plus the holes in the valence band. From now on, both electrons and holes can be called as carrier.

Semiconductor materials with no impurities added are called intrinsic materials and the number of carriers inside these materials is called intrinsic carrier concentration.

The band gap and the temperature of the material are factors that will affect the intrinsic carrier concentration. A small band gap and high temperatures will increase the intrinsic carrier concentration.

One fundamental technique used in semiconductor materials to vary the number of electrons and holes is named doping.

For example, *n*-type Silicon based semiconductors are produced by introducing atoms from elements in the group V in the periodic table to the intrinsic semiconductor. These elements have 5 valence electrons which can form covalent bonds. Silicon needs 4 valence electrons so the extra one will participate in conduction. By using elements from the III group in the periodic table, *p*-type material will be produced. In this case, only 3 valence electrons are present and the result is an extra hole. In *n*-type materials the majority carrier will be electrons (higher concentration) and in *p*-type material the majority carrier will be holes instead.

When photons of a light source come into contact with the surface of the semiconductor material, they can generate a pair electron-hole if the energy of the photon is equal or

greater than the band gap energy of the material. In this case, one electron from the valence band will be excited to the conduction band.

Different semiconductors have different absorption coefficients depending on how deep the photons are able to penetrate in the material before being absorbed.

The number of electrons generated at every single point in the semiconductor material due to the absorption of photons is called generation rate. In every semiconductor, different generation rates will be seen for different light wavelengths.

The opposite of generation will happen when electrons lose energy and fall into the valence band recombining with a hole. This process is called recombination [11].

### 1.1.2 *p-n* junction formation

When a *p*-type and an *n*-type semiconductor material are joined together, the *p-n* junction is formed. In the zone where the two materials are in contact, a combination of electrons from the *n*-type and holes from the *p*-type is formed by diffusion producing what is called depletion zone. The fixed ion cores left behind generate an induced electric field which can influence the movement of minority carriers. At the same time, minority carriers can reach the junction and move through the depletion zone due to drift. At equilibrium, diffusion and drift are compensated producing a net current of zero.

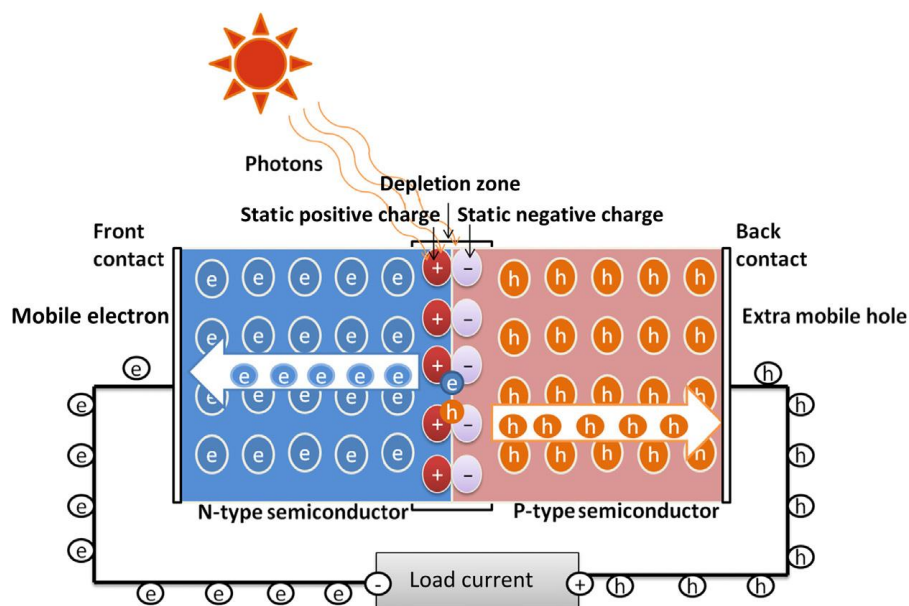


Figure 1.2 Diagram of a *p-n* junction photovoltaic solar cell [12]

When the  $p-n$  junction is under illumination, photons can be absorbed producing electron-hole pairs that will result in an excess of mobile charged carriers (see Figure 1.2). The extra mobile carriers will be transported and collected in the electrodes generating electrical current [13].

The characterization of a solar cell is determined through three different parameters. The short-circuit current ( $I_{SC}$ ) is the current that passes through the solar cell when there is no voltage across the solar cell. In the ideal case,  $I_{SC}$  is equal to the light-generated current. Due to this,  $I_{SC}$  is the maximum current produced in a solar cell.

The open-circuit voltage ( $V_{OC}$ ) occurs when the current in the solar cell is equal to zero and it is the maximum voltage achievable in the solar cell.

$$V_{OC} = \frac{kT}{q} \ln\left(\frac{I_L}{I_0} + 1\right) \quad (1.1)$$

The third necessary parameter is fill factor ( $FF$ ) and is defined as:

$$FF = \frac{V_{mp}I_{mp}}{V_{OC}I_{SC}} \quad (1.2)$$

It determines the maximum power that can be extracted from the solar cell.

From these parameters, the energy-conversion efficiency can be deduced:

$$\eta = \frac{V_{OC}I_{SC}FF}{P_{in}} \quad (1.3)$$

Where  $P_{in}$  is the total power from the incident light.

Efficiency is the most used parameter to characterize solar cells and to compare them. It is defined as the ratio between the energy received in form of light and the extracted energy out of the solar cell. As the efficiency depends on the properties of the incoming light, it is essential to have standard conditions to compare different devices. The standard conditions used to measure terrestrial solar cells are AM 1.5 (integrated power of 1000 W/m<sup>2</sup>) and a temperature of 25 °C .

### 1.1.3 Efficiency limitations in solar cells

In order to build highly efficient solar cells, the upper limits of energy conversion efficiency must be considered. This efficiency limit can be obtained by using the laws of thermodynamics. The process of converting the energy emitted by the sun in usable work can be described through a reversible Carnot heat engine [14]. This is the most fundamental energy conversion efficiency limit and it does not consider any entropy losses. It needs the following input parameters: the heat flux and the entropy flux coming from the sun, and also it assumes a temperature the sun of 6000 K. The output parameters of the solar cell are then, usable work and heat flux emitted to the ambient. Using the Carnot model an efficiency equation can be expressed as:

$$\eta_C = 1 - \frac{T_{SC}}{T_{Sun}} \quad (1.4)$$

Where  $T_{SC}$  is the temperature of the solar cell [15].

Landsberg considered the sun and the solar cell black-bodies with entropy losses through transmission, generation and conversion leading to a new efficiency limit model. In this model, heat fluxes are replaced by radiation energies [14]. In Figure 1.3 two different cases are plotted, in one, the temperature of the solar cell is assumed to be equal to the ambient temperature. In the other case,  $T_A = 300$  K is assumed as ambient temperature while the temperature of the solar cell can vary.

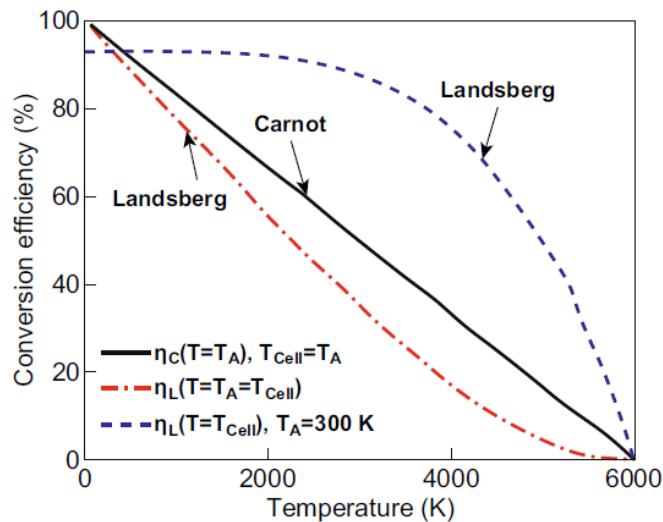


Figure 1.3 Carnot & Landsberg efficiencies at different temperatures [16]

**Ultimate conversion efficiency and theoretical Shockley-Queisser limit.** In 1961 William Shockley and Hans Queisser calculated for the first time the maximum limiting efficiency for a single  $p-n$  junction solar cell (multi-junction solar cells can outperform this limit). In the original work, 6000 K black-body spectrum was used as an approximation to the solar spectrum and modern revisions of this limit have used standard test conditions (STC) being 1000 W/m<sup>2</sup> of irradiance at 25 °C with an air mass 1.5 (AM 1.5) spectrum.

In the Shockley-Queisser (SQ) limit photons with energies higher than the band gap energy are absorbed while photons with energies below the band gap are not. In the ultimate conversion efficiency limit, only spectrum losses are considered and not losses through recombination of electron/hole pairs. After this assumptions, solar cells show a maximum conversion efficiency of 44% considering a temperature of 6000 K and 49% using AM 1.5 global spectrum.

An expansion of this model was done by adding losses through radiative emission by the solar cell, which means including the effects of recombination. The maximum energy conversion efficiency value is approximately 33.5% with a band gap of 1.2 - 1.4 eV while the ultimate efficiency limit reaches an optimal efficiency of 49% with a band gap of 1.1 eV [16].

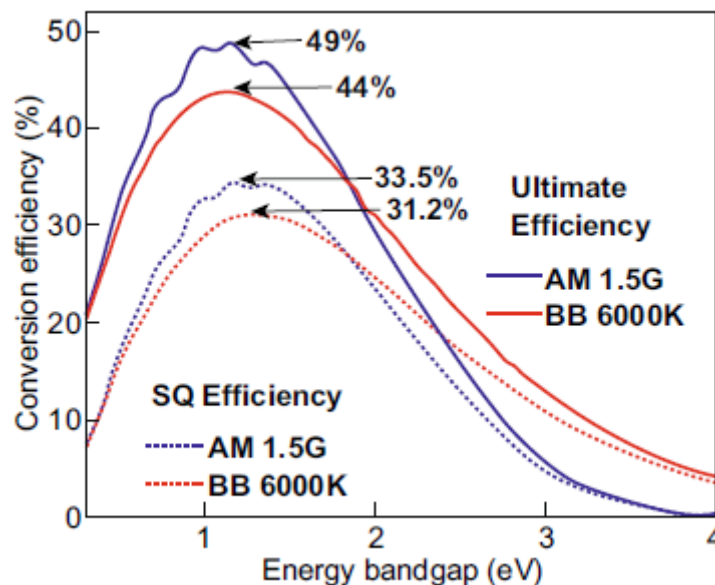


Figure 1.4 Ultimate efficiency limit and Shockley-Queisser limit of a single-junction solar cell for black-body spectrums of 6000 K and AM 1.5 [16]

**Effect of temperature in solar cells.** Several parameters in solar energy production are influenced by the effect of temperature. It has been seen experimentally that the output power of a crystalline solar cell can decrease by 0.66% as the temperature increases by 1 K with a drop in conversion efficiency of 0.08%/K. In the same experiment fill-factor decreased 0.2 %/K [17].  $V_{oc}$  also decreases when temperature increases [18].

## 1.2 Solar cell absorber materials - overview

The most important component in any solar cell is the absorber material. During the last half century, several different materials have been studied and developed to be used as absorber materials for solar cells. Absorber materials must fulfil some requirements to be considered ideal. A band gap between 1.1 and 1.7 eV, and as closer to 1.1 eV it is easier for an electron to be promoted from one band to another increasing the conduction of the material. Other important issue concerning absorber materials is the availability of their constituent elements, if the material is scarce, its price will be higher. Non-toxic materials are also preferable due to its interaction with the environment and disposing them will be less problematic. Simple fabrication techniques will also decrease the final cost of solar cells. The main effort goes through trying to increase the conversion efficiency and reduce production costs [19].

Solar cell absorber materials are usually classified into three different generations. In the first one, solar cells are wafer-based, made of crystalline silicon (c-Si), either polysilicon and monocrystalline silicon. Modern c-Si wafers can be in the range of 100-150  $\mu\text{m}$  thickness [20]. Commercial single crystalline solar cells can achieve efficiencies up to 20%. They are still the predominant PV technology in the market [12].

The second generation of solar cells uses thin film technology to reduce the material usage. Layers of materials used in thin film technology ranging from nanometres to several micrometres in thickness. They include different materials like amorphous silicon (a-Si), cadmium telluride (CdTe) and CIGS with conversion efficiencies of 7% [21], 22.1% [22] and 23.35% [23], respectively.

Third generation of solar cells include emerging photovoltaics, like organic solar cells (OSC) (18.5% of efficiency [24]), dye-sensitized solar cells (DSSC) (13.1% [25]), kesterite solar cells (CZTSSe) (12.6% [26]), perovskites (23.6% [27]) and quantum dots (16.6% [28]). Furthermore, tandem-based solar cells are used in this generation. They consist in solar cells with different layers of different materials having different

band gaps to absorb different light wavelengths, and achieving a higher efficiency as a result [29].

### **1.2.1 Kesterite based absorber materials**

Although chalcopyrite-based CIGS absorber material has reached an efficiency record of 23.35% [23], it requires the presence of rare-earth elements like In and Ga. Due to its scarcity and its high demand from the display industry, these elements tend to have a high price [30].

Kesterite materials  $\text{Cu}_2\text{ZnSnS}_4$  (CZTS),  $\text{Cu}_2\text{ZnSnSe}_4$  (CZTSe), and  $\text{Cu}_2\text{ZnSn}(\text{S},\text{Se})_4$  (CZTSSe) are an emerging group of materials intended to replace CIGS by substituting indium and gallium with more abundant and non-toxic elements like zinc and tin. Kesterites have similar properties with CIGS, that includes a similar band gap with a high absorption coefficient and both materials show *p*-type conductivity as a result of acceptor defects like copper vacancies and copper on zinc anti-site defects [31].

$\text{Cu}_2\text{ZnSnS}_4$  has a direct band gap of 1.5 eV and absorption coefficient ( $< 10^4 \text{ cm}^{-1}$ ). Its band gap can be tuned by altering the S/Se ratio between 1.0 and 1.5 eV for pure selenide and pure sulphide compounds, respectively [32].

The energy conversion efficiency of CZTSSe based solar cells has increased from 0.66% [33] in 1996 to 12.7% [4] in 2021, but it is still far from the theoretical 32% single-junction limit proposed by Shockley and Queisser [34].

### **1.2.2 Crystal structure**

Kesterite belongs to the compound family with  $A = \text{Cu}$ ,  $B = \text{Zn}$ ,  $\text{Fe}$ ,  $C = \text{Sn}$  and  $D = \text{S}$ ,  $\text{Se}$ . There are two tetragonal known structures from literature: The kesterite type structure and the stannite type structure. Both structures consist of a *ccp* array of anions and cations occupying one half of the tetrahedral voids. The difference between kesterite and stannite structures is in the distribution of copper and zinc atoms [35].

Kesterite type structure (see Figure 1.5 a) is characterized by alternating cation layers of Cu-Sn, Cu-Zn, Cu-Sn and Cu-Zn at  $z=0$ ,  $\frac{1}{4}$ ,  $\frac{1}{2}$  and  $\frac{3}{4}$  respectively. Stannite type structure Zn-Sn with  $\text{Cu}_2$  layers instead.  $\text{Cu}_2\text{ZnSnS}_4$  crystallizes in the kesterite type structure with space group being more stable than stannite type structure with space group [36].

The cation distribution plays a major role for kesterites. Cu/Zn disorder can cause vacancies and anti-site defects.

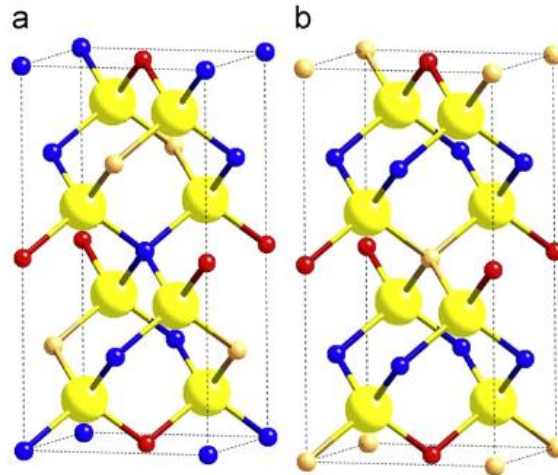


Figure 1.5 Unit cell representation of a) kesterite and b) stannite structure (Cu-blue, Zn-orange, Sn-red and S-yellow [36])

### 1.2.3 Phase diagram of CZTS

$\text{Cu}_2\text{ZnSnS}_4$  is a quaternary semiconducting compound consisting of three metals and a chalcogen. This leads to complicated phase diagrams with multiple phase formations. Figure 1.6 shows a vertical section of  $\text{Cu}_2\text{S}-\text{CZTS}-(\text{ZnS}+\text{SnS}_2)$ . The regions  $\alpha$ ,  $\beta$ ,  $\gamma$ ,  $\delta$  are solid solution regions of  $\text{Cu}_2\text{S}$ ,  $\text{ZnS}$ ,  $\text{SnS}_2$  and  $\text{Cu}_2\text{ZnSnS}_4$ , respectively. The grey area (11) in Figure 1.6 represents the single-phase area for CZTS. The temperature usually used for synthesis of the monograin powders is  $740^\circ\text{C}$  and it is marked on the graph with a grey horizontal line. The stability zone for the quaternary CZTS phase is about 2 mol% in composition which means that the process must be highly controlled as small variations in composition of  $\text{Cu}_2\text{S}$ ,  $\text{ZnS}$  and  $\text{SnS}_2$  will lead to non-desired secondary phases [37]. Secondary phases will cause a poor performance of solar cells based on inhomogeneous absorber materials [38].

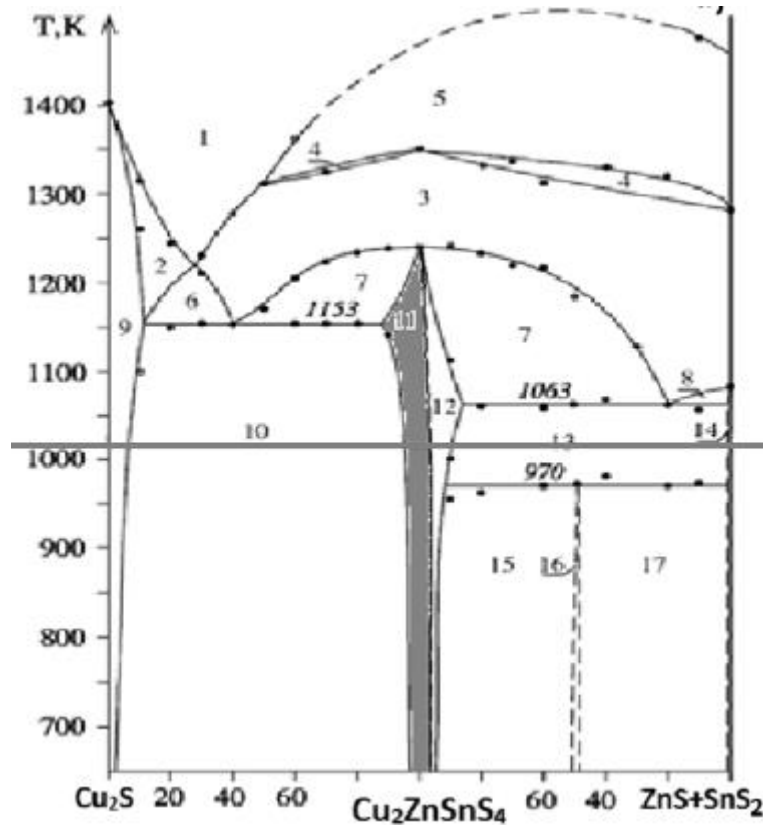


Figure 1.6 Phase diagram of the  $\text{Cu}_2\text{S}$ - $(\text{Cu}_2\text{ZnSnS}_4)$ - $(\text{ZnS}+\text{SnS}_2)$  section, where (1) L, (2)  $\text{L}+\alpha$ , (3)  $\text{L}+\beta'$ , (4)  $\text{L}+\beta+\beta'$ , (5)  $\text{L}+\beta$ , (6)  $\text{L}+\alpha+\beta'$ , (7)  $\text{L}+\beta'+\delta$ , (8)  $\text{L}+\beta'+\gamma$ , (9)  $\alpha$ , (10)  $\alpha+\delta$ , (11)  $\delta$ , (12)  $\beta'+\delta$ , (13)  $\beta'+\gamma+\delta$ , (14)  $\beta'+\gamma$ , (15)  $\beta'+\delta+\text{Cu}_2\text{ZnSn}_3\text{S}_8$ , (16)  $\beta'+\text{Cu}_2\text{ZnSn}_3\text{S}_8$ , (17)  $\beta'+\gamma+\text{Cu}_2\text{ZnSn}_3\text{S}_8$  [37]

### 1.2.4 Preparation methods of CZTS

The ratios of  $\text{Cu}/(\text{Zn}+\text{Sn})$  and  $\text{Zn}/\text{Sn}$  have an impact in the solar cell performance and to have highly efficient absorber material the Zn-rich and Cu-poor composition is necessary [39][40]. Several methods have been successfully used to synthesize the kesterite CZTS. In this section some of them will be commented.

In general, preparation methods of CZTS thin films can be classified into a vacuum process (evaporation, sputtering, chemical vapor deposition, etc.) and a non-vacuum process (spraying, spin coating, screen printing, electrochemical deposition, etc.).

The vacuum-based deposition methods have the following advantages: The chemical composition of CZTS thin films is relatively easy to control, it can be high reproducibility and thin films present a good quality. On the other hand, its deposition rate is slow and its production cost is high.

Non-vacuum deposition methods have a high growth rate and have a low production cost [41].

Electrochemical deposition is a process that consists in a thin coating of metal, oxide, or salt deposited onto the surface of a conductor or semiconductor substrate by electrolysis [42]. Thin film preparation using electrochemical deposition technique does not produce residual thermal stress between coating and substrate. Parameters such as coating thickness, chemical composition, structure and porosity can be highly controlled [43]. The equipment required is cheaper than other methods like evaporation, sputtering or chemical vapor deposition (CVD) [42][44].

Pulsed laser deposition method is a physical vapor deposition process, it uses high-power pulsed laser that focuses on a target's surface to produce high temperature and cauterization to then produce high pressure and high temperature plasma. Some of the advantages of pulsed laser deposition method include congruent transfer, crystallinity enhancement, virtually high-density arrival of species, cleaned deposition. This method is relatively simple and flexible in engineering design [45].

Sputter deposition technique is used to deposit thin films on substrates by bombarding with ions from a target. The most common approach consists in using a magnetron source. Positive ions present in the plasma of a magnetically enhanced glow discharge bombard the target [46]. Sputtering method offers some advantages like uniformity of films on large scale, high deposition rate. The process is also highly reproducible [47].

## **1.3 Post-treatment of CZTS**

### **1.3.1 Chemical etching**

During the synthesis process of CZTS monograin powders, at high temperatures (740 °C), part of the precursors and the synthesized kesterite dissolves in the flux. When the batch cools down to RT, part of the dissolved precursors precipitates on the surface of the formed CZTS monograins [39].

The devices with the best performance are Zn-rich and therefore they present an excess of zinc that allow secondary phases like ZnS to be formed. ZnS has a band gap of 3.54 eV and it behaves like an insulator being detrimental for the solar cell performance as it can reduce the active area generating less electron-hole pairs and therefore lowering the current value [48]. Sn-rich phases like SnS<sub>2</sub> with band gap of 2.2 eV will decrease

the open circuit voltage of the solar cells by forming a diode and barrier for carrier collection [49]. Both ZnS and SnS<sub>2</sub> are *n*-type secondary phases with a higher band gap than CZTS [6]. The presence of ZnS secondary phase will decrease the efficiency as well as  $V_{oc}$ ,  $J_{sc}$  and  $FF$  of CZTS solar cell devices [50]. Cu<sub>2</sub>S and Cu<sub>2</sub>SnS<sub>3</sub> ternary phase have a lower band gap than CZTS, 1.21 eV and 0.98-1.35 eV, respectively. Cu<sub>2</sub>S is metal like and highly defective chalcocite metallic and short circuits the solar cell while Cu<sub>2</sub>SnS<sub>3</sub> affects the carrier collection efficiency [48].

Altering the surface composition, or in other words, removing the non-desired secondary phases in kesterites is possible through different chemical etchings. It has been found that Bromine in methanol (Br<sub>2</sub>-MeOH) treatment followed by KCN treatment can improve the surface quality of the CZTS crystals [51]. KCN etching can selectively remove Cu-rich phases as Cu<sub>2</sub>S and to a lesser extent SnS<sub>2</sub> but no other secondary phases like ZnS [40][51]. Some experiments have shown that hydrochloric acid solution (HCl) can efficiently remove Zn-rich secondary phase like ZnS [52] and slightly Sn-rich phases [40]. Br<sub>2</sub>-MeOH etching mainly removes Cu and Zn-rich phases [53]. (NH<sub>4</sub>)<sub>2</sub>S etching can dissolve the Sn(S,Se)<sub>x</sub> secondary phase on the surface of CZTS according to Xie *et al.*[54].

### 1.3.2 Thermal treatment

Not only chemical treatments are used to improve the surface quality of the kesterites but also thermal treatments can be done to adjust the surface and bulk composition of quaternary compounds. Through thermal treatments it is possible to provide the required energy for atoms to diffuse to their equilibrium positions [37]. The thermal treatment process can be controlled by the temperature and atmosphere used.

If multinary compounds on a substrate are exposed to vacuum at elevated temperatures, interface reactions, reactions in the bulk and on the surface, can occur. The CZTS quaternary compound starts to decompose at 400 °C [39]. The most important interactions take place at the surface where the kesterite compound might decompose and release volatile material in form of gas as in the case of Sn (in the form of SnS) and S [55].



In case of CZTS the least stable element is Sn. At about 550 °C, tin sulphides decompose due to their volatility [55] but secondary phases like Cu<sub>2</sub>S and ZnS remain in the solid material (reaction 1.5) [37][56].



This reaction can be kept on the left side by heating the kesterite at isothermal temperature in a closed quartz ampoule with small volume or in presence of a controlled gaseous atmosphere. To avoid decomposition it is necessary to keep the sulfur pressure high enough during the annealing process [39].

Some models suggest not only the partial pressure of sulfur is necessary to avoid decomposition of CZTS at high temperatures but also the presence of SnS [57]. In addition, these models predict the decomposition of CZTS at maximum rate in the absence of a sulfur atmosphere, regardless of the partial pressure of SnS [58].

In several papers it has been shown that parameters of MGL solar cells are significantly affected by annealing temperatures and vapor pressures of the gaseous elements/compounds used. However, it is still not clear what the optimal parameters are regarding the post-annealing process of CZTS through different atmospheres [59].

Different gas atmospheres have also been used to anneal CZTS thin films. H<sub>2</sub>S atmosphere has been used to remove the formation of different impurities like different secondary phases. Singh *et al.* reported that the effect of annealing time in an H<sub>2</sub>S atmosphere can change the optical parameters of the CZTS material, like its band gap [60]. This is due to the amount of CuS secondary phase presented in the material. CuS band gap is different than CZTS one and the presence of this secondary phase will modify CZTS band gap. The presence of CuS decreased by increasing the annealing time. By increasing the annealing time the crystallite size increased [60].

As the overall stoichiometry of the CZTS is designed to be Zn rich, a higher concentration of the secondary phase ZnS is expected by annealing at high S partial pressure [52].

In order to control the phases and surface composition of CZTS during annealing step in a sulfur atmosphere, interface reactions and diffusion processes should be considered. In Figure 1.7 the schematic elemental diffusion routes and surface reaction mechanisms are shown. Copper is the element with the highest mobility and tends to diffuse into inner layers of the material giving a slightly Cu poor concentration on the bulk of CZTS. Zinc concentrates towards the surface due to the sulfurization giving a lower Cu/Zn ratio at the surface [61].

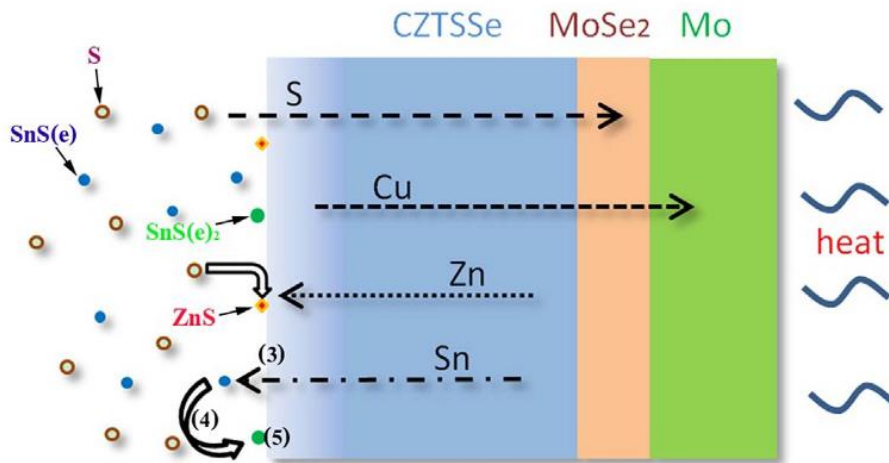


Figure 1.7 Diffusion routes of Cu, Zn, Sn and S in CZTS during annealing process in a S atmosphere [61]

In this work the effect of different post-annealing processes with different atmospheres and different conditions will be studied to improve the quality of CZTS MGP used as an absorber material in monograin layer solar cells.

## 1.4 Monograin powder technology

### 1.4.1 Monograin Powder Growth

Monograin powder materials with different compositions can be synthesized from elemental metals or metal binaries in a molten salt (flux) in an isothermal recrystallization process.

Single crystals or single-crystalline powders can be obtained at temperatures lower than the melting temperature of semiconductor itself and higher than the melting temperature of flux if they are used in the synthesis-growth process. Flux material used in the synthesis of powders is beneficial for several reasons. It increases the homogeneity of the solid product, and it controls the particle size, shape and their agglomeration state [39]. The characteristics of the monograin powder crystals can be controlled by selecting the synthesis temperature, time, the type of salt and its quantity [62]. The volume of the flux salt has to exceed the volume of the voids between precursor particles, otherwise formed powder particles and precursor particles can be sintered and that has to be avoided. Once the synthesis is complete, the used molten

salt can be removed by washing with a suitable solvent so the released powder can be dried and sieved (Figure 1.8).

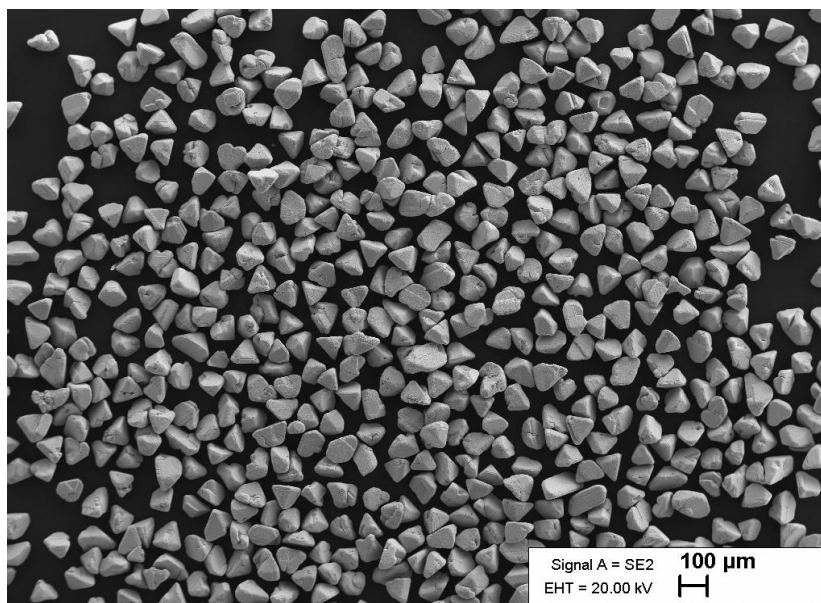


Figure 1.8 Monograin powder (MGP) of CZTS kesterite material (synthesized in this study)

The main advantage of monograin layer technology is that the absorber material can be fabricated separately from the production of the whole solar cell. Because of this, high temperatures can be used.

### 1.4.2 Monograin Layer Solar Cells

Planar and thin-film technologies are nowadays the most used technologies for manufacturing solar cells. Planar uses very expensive large 3D single crystals. Thin-film technologies reduce the amount of material to lower the price and in fact solar cells based on thin-film technologies are much cheaper than monocrystalline ones.

Monograin powder technology uses powder materials to form absorber layers. The main advantage of this technology lies in its simplicity of making single-crystalline large-area layers. Generally, this technology tends to be cheaper than the planar and thin-film technologies and it allows the possibility of using cheap, flexible and low temperature substrates to produce flexible cheap photovoltaic devices [62][63].

A typical monograin layer (MGL) solar cell consists in one single thick layer of grains of monograin powder embedded into an organic resin (epoxy). The MGL solar cells have

the following structure: graphite/MGP absorber layer/CdS buffer/i-ZnO/ZnO:Al window layer/Ag/glass (see Figure 1.9). In this study, MGP absorber material is CZTS kesterite material [39].

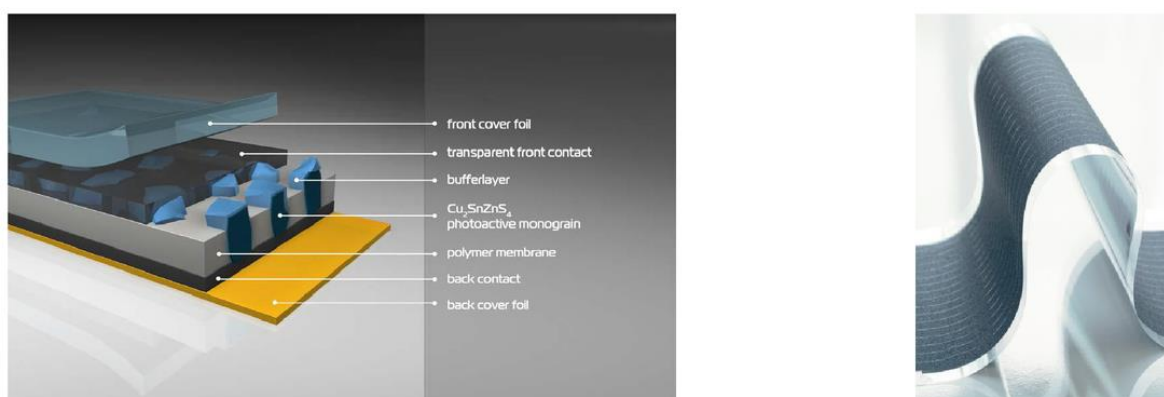


Figure 1.9 Scheme of the monograin membrane comprising CZTS crystals (left), photo of a monograin membrane (right) [64]

## 1.5 Summary of the literature review and the aim of the study

Photovoltaic energy is expected to play an important role in reducing greenhouse gas emissions by increasing its annual production capacity during the following years. Solar cells need to be more efficient and durable but at the same time scarce and toxic materials must be substituted for more abundant and cheaper ones. Even if silicon based solar cells are still ahead in the market, new materials and technologies are currently being investigated. Kesterite materials like  $\text{Cu}_2\text{ZnSnS}_4$ ,  $\text{Cu}_2\text{ZnSnSe}_4$ , and  $\text{Cu}_2\text{ZnSn}(\text{S},\text{Se})_4$  are intended to replace  $\text{Cu}(\text{In},\text{Ga})\text{Se}_2$  solar cells by substituting scarce Indium and Gallium with more abundant and environmentally friendly elements like Zinc and Tin. CZTS has a direct band gap of 1.5 eV and an absorption coefficient ( $< 10^4 \text{ cm}^{-1}$ ) which makes it a promising absorber material candidate for solar cells. The efficiency of kesterite based solar cells has increased from 0.66% to 12.7% in the last two decades but is still quite low compared with CIGSe thin film solar cells. CZTS can be synthesized by different methods (evaporation, sputtering, CVD, electrochemical deposition, etc.). The properties and quality of the absorber material depend on the preparation technology and directly affect the efficiency of  $\text{Cu}_2\text{ZnSnS}_4$  solar cells.

CZTS used in this work has been synthesized from metal binaries in a molten salt in an isothermal recrystallization process to obtain a monograin powder. Through the monograin powder technology, absorber layers can be produced to form MGL solar cells. They consist in a single thick layer of grains of monograin powder crystals embedded into an organic resin. In the molten salt synthesis-growth process, the initial precursors and the formed compound crystals dissolve in the molten salt at the level of their solubility at the growth temperature. After the CZTS synthesis-growth process, some part of the material dissolved in the molten salt at growth temperature deposits onto surfaces of the formed crystals during the cooling period. In order to improve the surface quality of the monograins, different post-treatments have to be carried out. That includes chemical etching with bromine in methanol followed by etching with KCN. Other chemicals can be used to etch different secondary phases. Also, thermal post-treatment has been found to be useful to heal the monograins after synthesis-growth and etching process.

The objective of this work is to modify the bulk and surface composition of  $\text{Cu}_2\text{ZnSnS}_4$  monograin powder crystals by different post-annealing treatments in sulfur-containing atmosphere with the aim to study the impact on the solar cell parameters.

## 2. METHODOLOGY

The  $\text{Cu}_{1.84}\text{Zn}_{1.09}\text{Sn}_{0.99}\text{S}_4$  monograin powders used in this study were synthesized from high purity (99.999%) binary precursors CuS, SnS and ZnS in the liquid phase of KI (99.99%). As flux material, water-soluble potassium iodide was used with the volume ratio of liquid KI to solid CZTS equal to 1 ( $\text{cm}^3/\text{cm}^3$ ). The precursors were weighed in desired amounts and ratios, mixed in a ball mill and loaded into quartz ampoules. The ampoules with powder batches were degassed under dynamic vacuum, sealed and heated isothermally at 740 °C for 144 hours. After cooling the ampoules to room temperature, the flux material was removed by leaching and rinsing with deionized water. The released monograin powders were dried in a hot-air oven at 50 °C and sieved into several narrow granulometric fractions between 38 to 125  $\mu\text{m}$  by sieving system Retsch AS 200. Unisize crystals were used in the post-treatment experiments.

### 2.1 Post-treatments of asgrown monograins

#### 2.1.1 Chemical etchings of monograin powder crystals` surfaces

Before the post-annealing process, all the samples were etched 5 min with 1% (v/v) bromine in methanol ( $\text{Br}_2\text{-MeOH}$ ) and also 5 min in 10% (m/m) aqueous solution of KCN at room temperature. The reason of this etching was to remove non-desired secondary phases from the MGP crystals` surfaces. The powders were washed several times in deionized water ( $\text{DI-H}_2\text{O}$ ) after the etching process and dried in a hot-air oven at 50 °C.

#### 2.1.2 Post-annealing in different atmospheres

The post-annealing was done inside a two-temperature zone furnace. For that, the CZTS powder was first introduced in one side of a quartz ampoule with an additional vapor source (elemental sulfur pellets) in the other side as it can be seen in Figure 2.1. The volume of used ampoule was  $\approx 20 \text{ cm}^3$  with inside diameter of 0.9 cm and length of 32.5 cm. The temperature of the two different zones was controlled independently. For adding sulfur, the amount of sulfur was calculated from the ideal gas law,  $PV = nRT$ , to satisfy the formation of saturated vapor pressure throughout the free volume of the two-zone ampoule. The amount of added S exceeded that to ensure an inexhaustible source of S (not fully vaporized amount of S).

The temperature of the material side was set between 550 and 850 °C and the vapor pressure of the sulfur between 100 and 2050 Torr (330 and 550 °C). All the different combinations of temperatures were annealed for 20 and 60 minutes. Material temperature should be always slightly higher than the component one to prevent the component precipitation on the material.

After the annealing process, the ampoules were removed from the furnace and cooled down to room temperature.

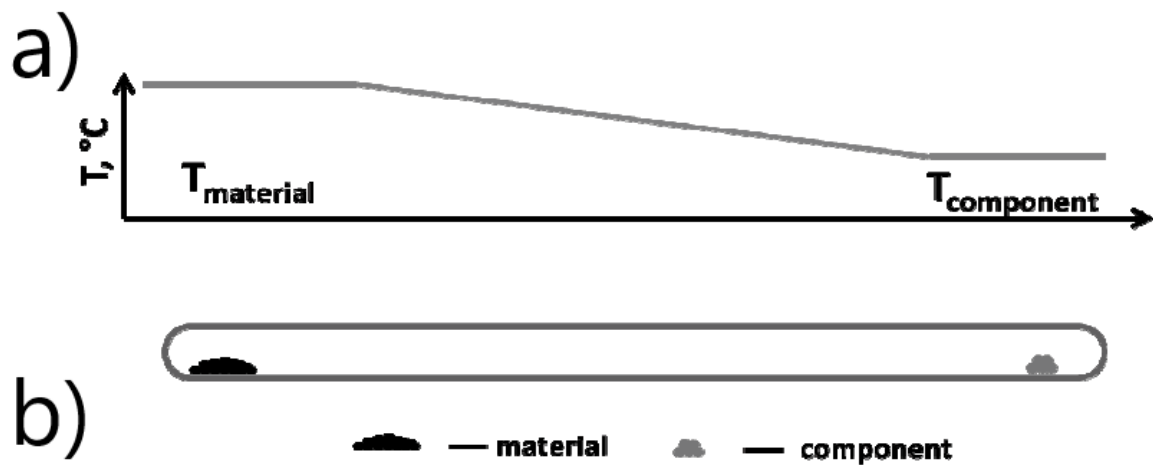


Figure 2.1 Temperature profile inside the two-zone furnace. b) Distribution of the materials inside the closed ampoule [37]

In total, 24 experiments were carried out by changing the material temperature, the sulfur pressure and the annealing time as seen in the Table 2.1

Table 2.1 Conditions for post-annealing in a sulfur atmosphere

$T_{mat}$ , °C	Sulfur pressure/temperature Torr/°C	Time, min	Experiment number
550	100/330	20	1
		60	2
	1000/465	20	3
		60	4
	2050/550	20	5
		60	6
650	100/330	20	7
		60	8
	1000/465	20	9
		60	10
	2050/550	20	11
		60	12
750	100/330	20	13
		60	14
	1000/465	20	15
		60	16
	2050/550	20	17
		60	18
850	100/330	20	19
		60	20
	1000/465	20	21
		60	22
	2050/550	20	23
		60	24

After the post-annealing and before deposition of CdS as buffer layer, the samples were etched 15 seconds in 1% (v/v) Br<sub>2</sub>-MeOH followed by 30 seconds of 10% (m/m) aqueous solution of KCN etching. Before the deposition of the buffer layer the phase composition of the post-annealed powder crystals' surfaces was analyzed by room-temperature (RT) micro-Raman spectroscopy.

One more experiment was carried out where not only sulfur but Argon as inert gas was also added in the quartz ampoule. Four different argon vapor pressures of 10, 50, 100 and 300 Torr were used.

## 2.2 Preparation of MGL solar cells

After the post-treatment of the monograin powders, the CdS buffer layer is deposited on the CZTS crystals through chemical bath deposition (CBD). After *n*-type buffer layer preparation, the monograins are embedded into a layer of epoxy resin, leaving part of the grains exposed. Then, the membranes are covered with intrinsic ZnO (i-ZnO)

followed by aluminum doped ZnO (ZnO:Al) as a conductive window layer by using a radio frequency magnetron sputtering. Finally, to intensify the collection of charge carriers, the conductive silver paste is used as the front contact and the solar cell structure is glued onto a soda lime glass plate. Before the application of the back contact (graphite), part of the epoxy resin is removed by etching with concentrated  $H_2SO_4$  (to release the surface of powder crystals from the epoxy) and polished with sandpaper to open the back contact area of crystals. A hole is made on the back side of the solar cell and filled with silver paste to bring the front contact to the back side for the solar cell characterization by  $I-V$  curve measurements. After that, an adhesive template is fixed on the solar cell. It consists in six similar circular empty shapes where the graphite paste as back contact was added. After the application of the graphite, the template is removed and the solar cell is complete and ready for the characterization (Figure 2.2).

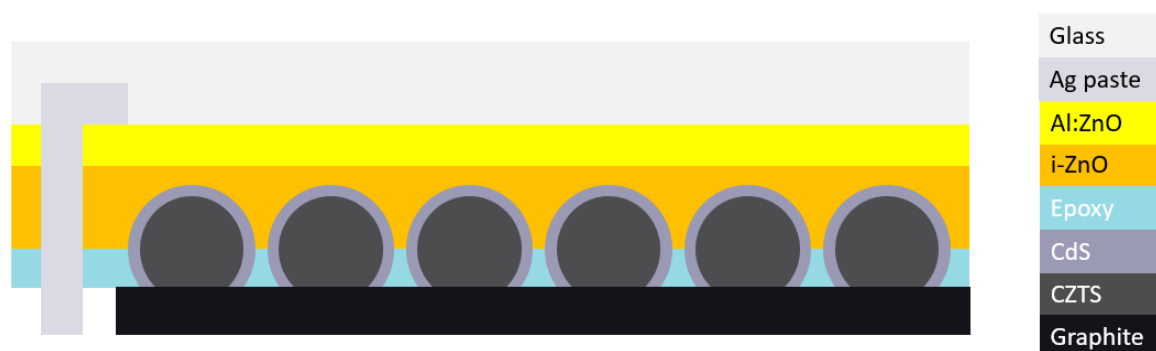


Figure 2.2 Schematic structure of CZTS MGL solar cell

## 2.3 Characterization of monograin powders and monograin layer solar cells

### 2.3.1 Energy Dispersive X-ray Spectroscopy (EDX)

Energy dispersive x-ray spectroscopy is an analytical method for identifying and quantifying elemental composition of materials [65].

EDX is based on the emission of characteristic x-rays of specific specimens. A beam of high energy charged particles is used to bombard the material to be investigated. When electrons from the beam hit the sample, atoms close to the surface are excited and emit specific wavelengths of x-rays. These x-rays are characteristic of the atomic structure of the elements present in the sample [66].

EDX analysis will give information about the elemental composition of the material through the spectrum that displays the peaks correlated to the different elements belonging to the sample [65].

To determine the elemental composition of the powders (polished cross-section of powder crystals, at least 10 in every sample were analyzed) used for monograin layer solar cells, Bruker Esprit 1.82 EDX system equipped with Röntec EDX XFlash 3001 detector with an accelerating voltage of 20 kV (the measurement error is about 0.5 at. %) was used. The EDX measurements were carried out by Dr. Valdek Mikli in Tallinn University of Technology.

### **2.3.2 Scanning Electron Microscopy (SEM)**

The scanning electron microscopy is a technique that uses an electron beam that produces a topological image and gives information about the relative chemical composition by interacting with the desired material.

When the sample is bombarded by the electron beam, low-energy secondary electrons (SE) can be emitted producing an inelastic interaction. These electrons are collected and processed in the electron detector and displayed in the computer. SE is the most common type of signal used in SEM analysis and it provides information about the morphology of the surface of the studied material as SE signal comes from the most outer layers of the sample (few nm) [67]. Not only SE can be detected but also back scattered electrons (BSE) can be used in SEM analysis. These electrons have greater energies than SE and come from deeper layers in the sample. They will provide chemical compositional contrast [67].

Several SEM images of the as-grown and post-treated powders were taken to study their morphology. A ZEISS HR SEM ULTRA 55 with In-lens secondary electron detection at accelerating voltage of 4 kV was used. The SEM measurements were carried out by Dr. Valdek Mikli in Tallinn University of Technology.

### **2.3.3 Room Temperature Micro-Raman Spectroscopy**

Raman spectroscopy is a non-destructive chemical analysis technique that provides information about the chemical structure of a material, phase and polymorphism as well as contamination and impurities [68].

Raman spectroscopy is a powerful tool for determining crystalline structure and quality of semiconductor thin films, since the shape and position of Raman peaks are strongly influenced by the presence of defects in the material such as secondary phases. It can be used as a control method to identify the different secondary phases present in a semiconductor like the CZTS absorber material [69].

It is based on inelastic scattering of monochromatic radiation and the molecular media. When the photon interacts with a molecule, the energy is exchanged and the scattered phonon has a higher or lower energy than the incident one. This difference in energy is produced by a change in the rotational and vibrational energy of the molecule and it can provide information about its energy levels [70].

Raman spectroscopy was used to study the phase composition of as-grown and post-treated powders crystal surfaces. The apparatus used was a Horiba's LabRam HR spectrometer equipped with a 532 nm laser line focused on the sample with a 5  $\mu\text{m}$  size spot.

### **2.3.4 Current-Voltage (*I-V*) Characterization**

The MGL solar cells were analyzed by measuring the current density vs voltage characteristics in light and in dark. Keithley 2400 electrometer and Newport solar simulator was used under standard test conditions (AM 1.5, 100  $\text{mW}/\text{cm}^2$ ). From the *I-V* curves different parameters were calculated by a program built in LabVIEW: the solar energy conversion efficiency ( $\eta$ ), short-circuit current density ( $j_{sc}$ ), open-circuit voltage ( $V_{oc}$ ), and fill factor (*FF*).

Six different regions of every solar cell were measured. They were determined by six spots forming a line where the graphite paste was applied in the first series (annealing in sulfur atmosphere) and evaporated gold contacts were used in second series (annealing in sulfur plus argon atmosphere). As mentioned before, they all have the same shape and area. In case of gold contacts, a square shaped grid is measured. Due to the epoxy between MGP crystals in the membrane, the working area of the MGL solar cells is around 75% of the total area. Therefore, the MGL solar cell efficiency values were re-calculated for the active area ( $\eta_{active}$ ).

### **2.3.5 Quantum Efficiency (QE) Measurements**

The quantum efficiency of a solar cell is defined as the ratio of the number of electrons in the external circuit produced by an incident photon of a determined wavelength or in other words, the total current produced when the solar cell is exposed to a light of a certain wavelength [71]. Two different quantum efficiencies can be defined as external quantum efficiency (EQE) and internal quantum efficiency (IQE). EQE is the ratio between all the charge carriers collected by the solar cell with the number of the total incident photon while in IQE, only the absorbed photons, the ones not reflected are included [72]. In this work EQE measurements has been performed in the spectral region of 350-950 nm using a computer-controlled SPM-2 prism monochromator. The generated photocurrent was detected at 0 V bias voltage at RT by using a 250 W halogen lamp. The EQE measurements were carried out with the assistance of Dr. Mati Danilson.

### **2.3.6 Electron Beam Induced Current (EBIC) measurements**

In solar cells, photons provide the required energy to create electron-hole pairs that due to drift and through the electric field of the SC will contribute to the flow current. In EBIC, an electron beam substitutes the photons providing energy. In this way, parts of the material where electrons can be collected will appear bright while the parts where electrons are recombined and therefore do not contribute to the current will appear dark. EBIC can be used together with SEM to investigate defects in solar cells [73].

Electron Beam Induced Current measurements were performed by using a Merlin, Carl Zeiss Microscopy, Germany. EBIC mapping was performed by specimen current amplifier, model - Type 31, GW Electronics Ins., USA. The accelerating voltage of 20 kV for surface EBIC was used. The EBIC measurements were carried out by Dr. Olga Volobujeva in Tallinn University of Technology.

## 3. RESULTS AND DISCUSSION

### 3.1 Post annealing in sulfur atmosphere

After the chemical etching, CZTS monograin powders were annealed in a two-zone furnace at different material temperatures, sulfur vapor pressures and annealing times. See Table 2.1

#### 3.1.1 Morphology of the CZTS monograins after post-annealing in sulfur atmosphere

To analyse the surface morphology of the different grains, several SEM images were taken from 12 of the 24 experiments done. Only the morphology of the samples with annealing times of 60 minutes have been studied. The crystals have tetrahedral shape and sharp edges as can be observed in the different SEM images (see Figure 3.1). The shape of the grains remains the same after both chemical and annealing treatments in all different conditions. The surface of the as-grown monograins Figure 3.2a is covered by different precipitations that will be removed after the chemical etching. The etched crystal surface is rougher. After annealing, the etched crystal surface is well-formed crystalline (Figure 3.1b and Figure 3.2b-d). The changes in surface morphology of the grains take place during the chemical etching but it does not change with the different thermal treatment regimes.

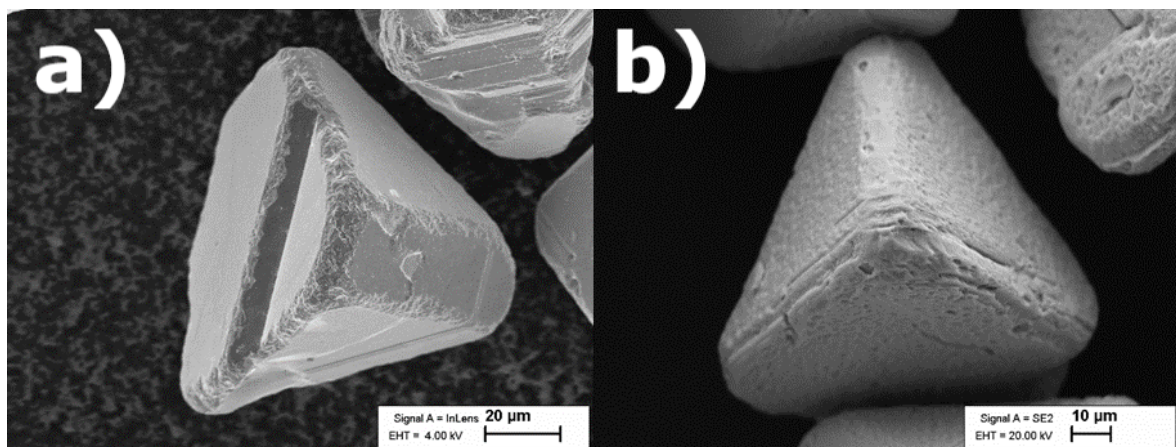


Figure 3.1 SEM image of CZTS monograin powder (left) as-grown crystals and (right) etched and annealed at  $T_{\text{mat}} = 550 \text{ }^{\circ}\text{C}$ ,  $T_{\text{comp}} = 550 \text{ }^{\circ}\text{C}$  (at 2000 x magnification)

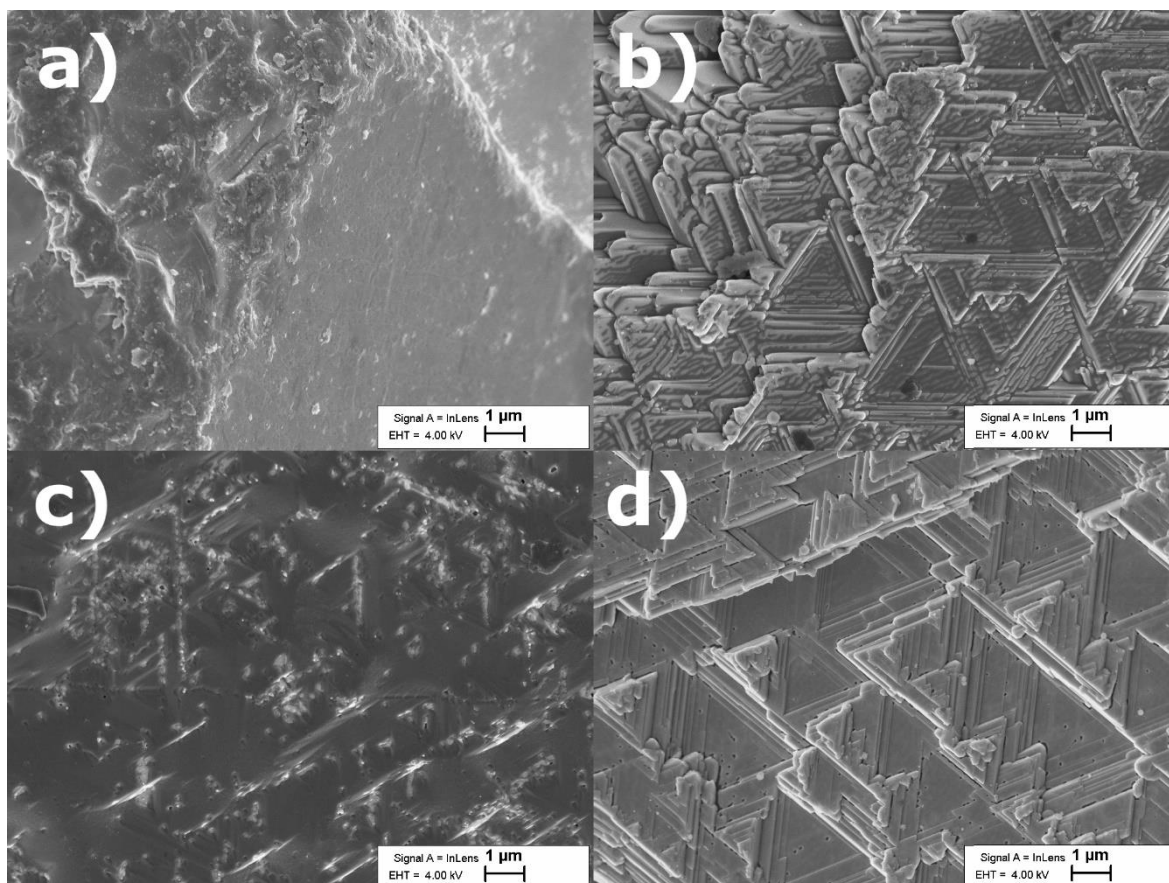


Figure 3.2 SEM images of CZTS crystals' surfaces (at 20000 x magnification): (a) as-grown; and after etching plus annealing at (b)  $T_{mat} = 550\text{ }^{\circ}\text{C}$ ,  $T_{comp} = 330\text{ }^{\circ}\text{C}$ ; (c)  $T_{mat} = 750\text{ }^{\circ}\text{C}$ ,  $T_{comp} = 465\text{ }^{\circ}\text{C}$ ; and (d)  $T_{mat} = 850\text{ }^{\circ}\text{C}$ ,  $T_{comp} = 465\text{ }^{\circ}\text{C}$

SEM images revealed the light areas on the powder crystal surfaces after the post-annealing under determined sulfur pressure as seen in Figure 3.3a-b and Figure 3.4d. Herein, it must be pointed out, that the light areas on the crystal surfaces were found by SEM only on some crystals' surfaces and are not seen always after post-annealing in sulfur atmosphere. Therefore, the reason of their formation is unclear and further studies are needed.

In addition to the formed light areas on crystals' surfaces, layers of  $\text{SnS}_2$  as secondary phase are also determined on the crystals' surfaces by SEM and EDX. They have different sizes and appear darker (Figure 3.4a-d). While light areas content is quite low and barely detectable,  $\text{SnS}_2$  is very well detectable by SEM and easy to analyze by EDX (see Figure 3.4a, c, d and Table 3.1).

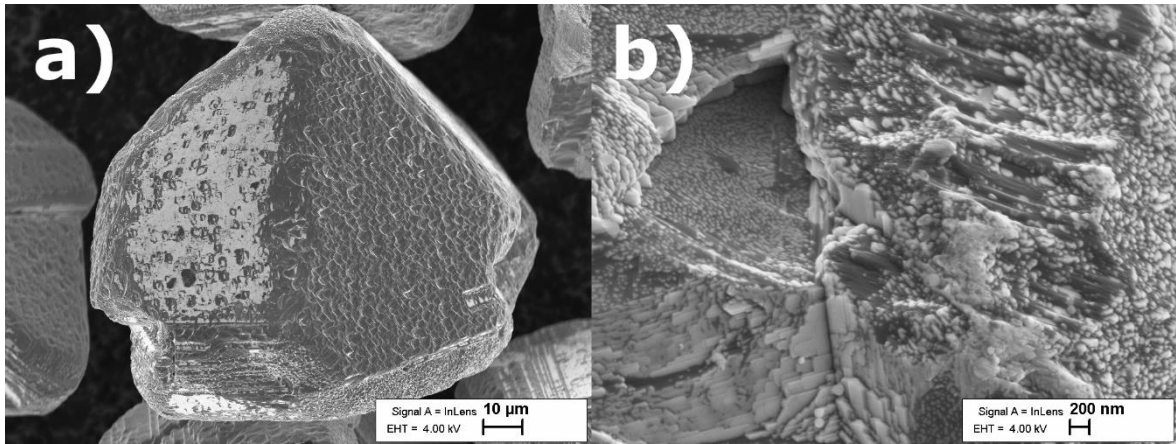


Figure 3.3 SEM images of ZnS secondary phases on CZTS crystals` surfaces (a) annealed at  $T_{mat} = 750 \text{ }^\circ\text{C}$ ,  $T_{comp} = 330 \text{ }^\circ\text{C}$  (at 2000 x magnification); (b)  $T_{mat} = 850 \text{ }^\circ\text{C}$ ,  $T_{comp} = 330 \text{ }^\circ\text{C}$  (at 50000 x magnification)

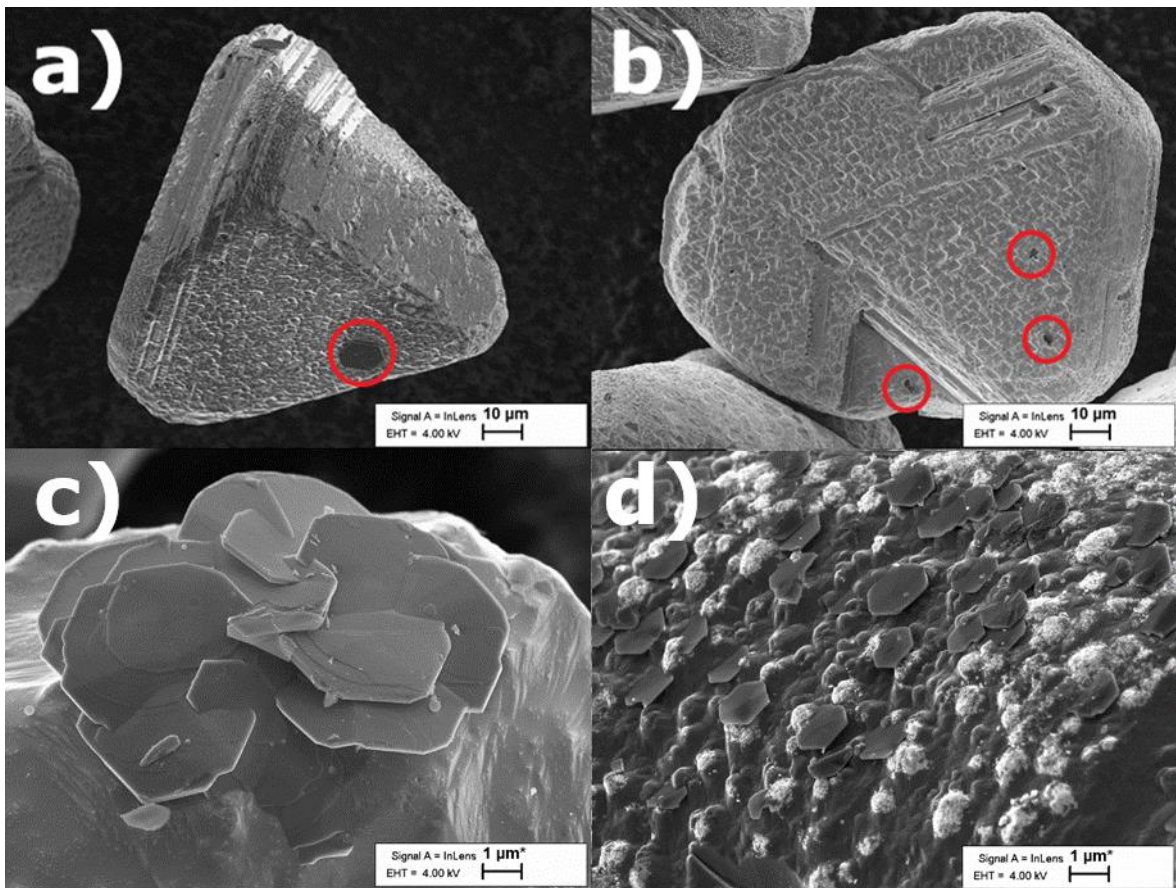


Figure 3.4 SEM images of SnS<sub>2</sub> secondary phases on CZTS crystals` surfaces (a) annealed at  $T_{mat} = 650 \text{ }^\circ\text{C}$ ,  $T_{comp} = 330 \text{ }^\circ\text{C}$  (at 2000 x magnification); (b)  $T_{mat} = 850 \text{ }^\circ\text{C}$ ,  $T_{comp} = 465 \text{ }^\circ\text{C}$  (at 2000 x magnification); (c)  $T_{mat} = 850 \text{ }^\circ\text{C}$ ,  $T_{comp} = 550 \text{ }^\circ\text{C}$  (at 20000 x magnification); and (d)  $T_{mat} = 650 \text{ }^\circ\text{C}$ ,  $T_{comp} = 465 \text{ }^\circ\text{C}$  (at 20000 x magnification)

The EDX elemental mapping of Sn, Zn and Cu at post-annealed CZTS crystal surface is presented in Figure 3.5. The EDX elemental mapping shows the Sn-rich areas on

crystals` surfaces (by confirming SnS<sub>2</sub> locations as a secondary phase), while the Cu and Zn contents decreased at the same areas.

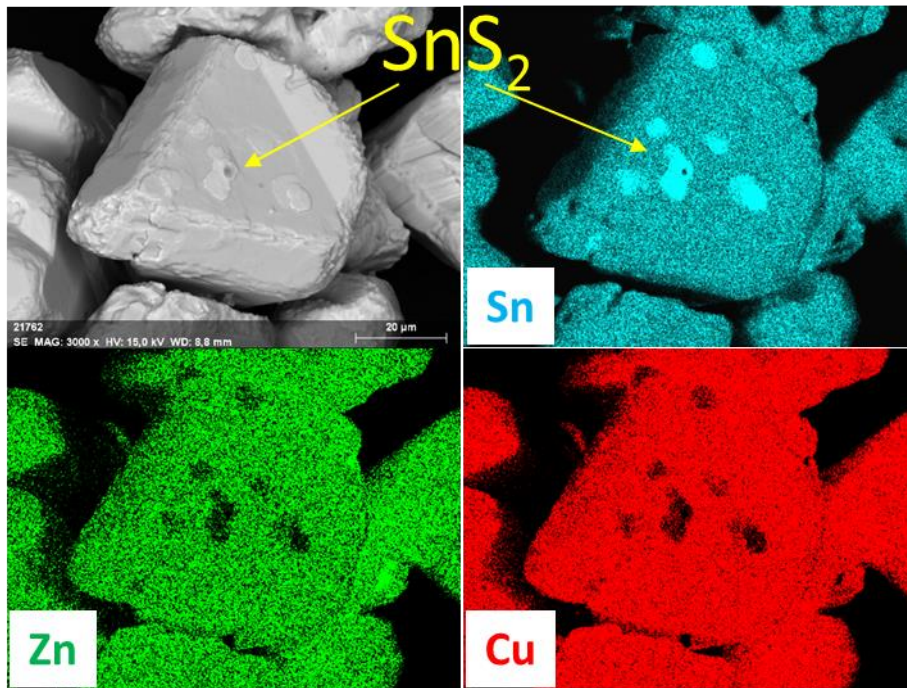


Figure 3.3 SEM image and EDX elemental mapping of Sn, Zn, Cu from post-annealed CZTS crystal surface

### 3.1.2 Phase composition of Cu<sub>2</sub>ZnSnS<sub>4</sub> monograin powder crystals` surfaces after post-annealing in sulfur atmosphere

SEM images of the different monograin powders suggest the presence of different secondary phases on the crystals` surface. EDX analysis has been carried out to measure the elemental composition of these secondary phases. In Figure 3.6, two regions can be differentiated on CZTS surface. The elemental compositional analysis of these small particles (areas 2 and 3) suggest that they belong to the secondary phase SnS<sub>2</sub> and not to the main kesterite phase (area 1). See Table 3.1.

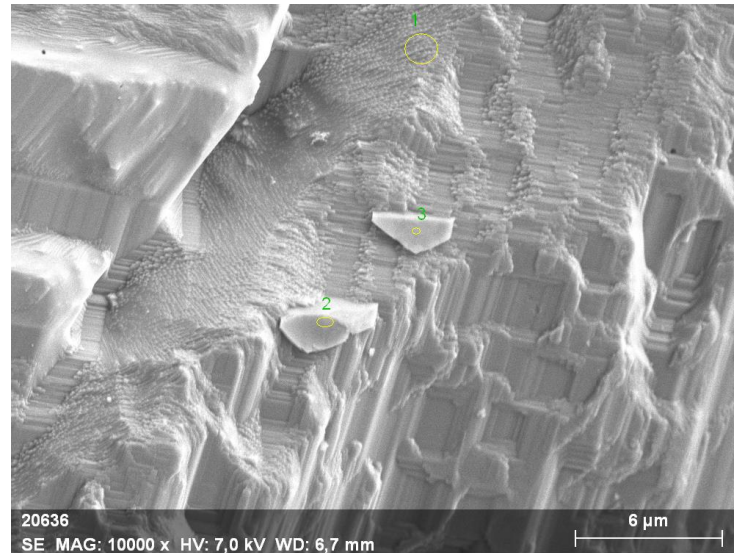


Figure 3.4 SEM image of CZTS monograin powder crystal surface after chemical etching and annealing at  $T_{\text{mat}} = 850 \text{ }^\circ\text{C}$ ,  $T_{\text{comp}} = 550 \text{ }^\circ\text{C}$

Table 3.1 Chemical composition of CZTS monograin powder crystal surface in different areas (Figure 3.6)

Analysis No.	Cu, at.%	Zn, at.%	Sn, at.%	S, at.%
1	34.1	16.9	9.4	39.6
2	4.5	2.9	31.3	61.4
3	16.9	8.0	21.1	54.1

Figure 3.7 shows the Raman spectra of CZTS monograin powders: as-grown, etched with bromine in methanol followed by etching with 10% KCN aqueous solution, and after annealing at different regimes ( $T_{\text{mat}} = 550$  and  $650 \text{ }^\circ\text{C}$ ;  $T_{\text{comp}} = 330, 465$  and  $550 \text{ }^\circ\text{C}$ ) in sulfur atmosphere. The numbers in parenthesis in Figure 3.7 correspond to the material temperature and component (sulfur) temperature during the annealing process. The Raman spectra of the all measured powders show the main peaks at 96, 146, 252, 288, 338, 362 and  $375 \text{ cm}^{-1}$ . These peak positions correlates well with the CZTS Raman spectra from the literature measured with laser wavelength of 532 nm [74]. The results of Raman analysis do not show the presence of other secondary phases after post-treatment except in one case, where the material was annealed at  $T_{\text{mat}}=550 \text{ }^\circ\text{C}$ ,  $T_{\text{comp}}=550 \text{ }^\circ\text{C}$  (2050 Torr) and peak at  $342 \text{ cm}^{-1}$  revealed. The origin of this peak is unknown. Even if the material temperature was set to be slightly higher than the component one, as the temperatures are not constant and because of their fluctuation, it may had happened that the temperature of the component side was higher in some moments and for this reason, some secondary phases formed in gas phase could

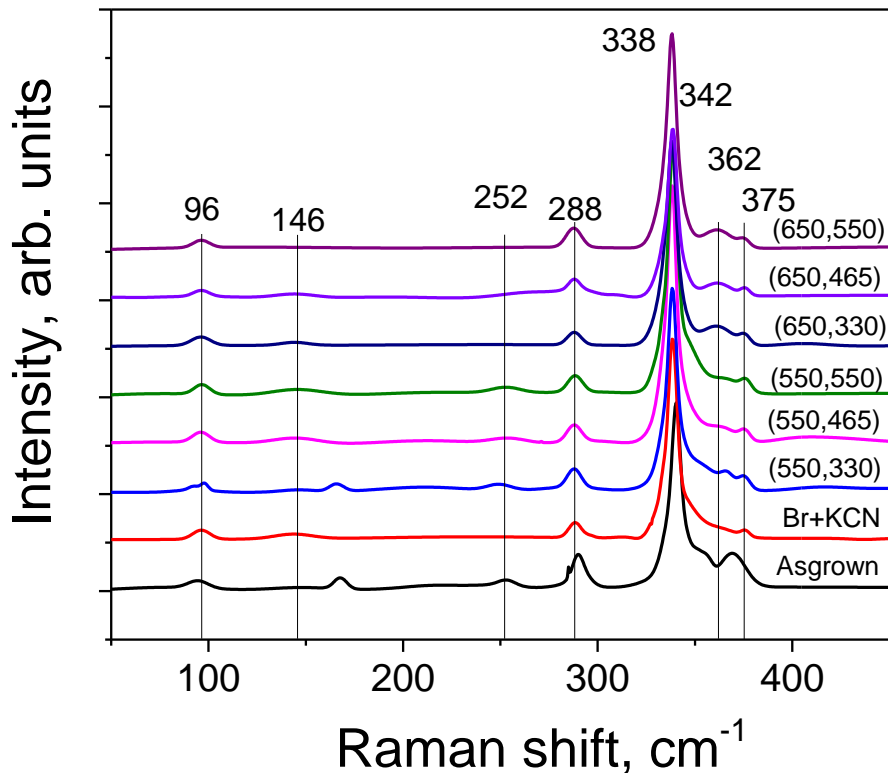


Figure 3.5 Raman spectra of CZTS monograin powders: As-grown, etched with 1% Br<sub>2</sub>-MeOH followed by 10% KCN etching and annealed for 60 minutes at different post-annealing regimes ( $T_{\text{mat}} = 550$  and  $650$  °C,  $T_{\text{comp}} = 330$ ,  $465$  and  $550$  °C)

precipitate on the crystals` surfaces. In general, we can say that the phase composition of our material did not change for these annealing conditions.

Raman spectra of CZTS MGPs annealed at regimes  $T_{\text{mat}} = 750 - 850$  °C and  $T_{\text{comp}} = 330 - 550$  °C were similar with spectra presented in Figure 3.8 except for the regime  $T_{\text{mat}} = 850$  °C;  $T_{\text{comp}} = 330$  °C (100 torr). In this case orange well-formed tiny crystals were seen in the middle of the treatment ampoule after post-treatment experiments. Most probably the vapor pressure was not high enough and the material started to decompose.

Secondary phase belonging to ZnS could not be detected probably due to the wavelength of the laser used during Raman analysis in TalTech. It is needed a blue laser of 325 nm to detect ZnS. In addition, also SnS<sub>2</sub> secondary phase could not be found in Raman spectra measured in TalTech, but that can be attributed to the fact that the laser used for analyzes had spot size of about 5 μm and it is optically difficult to focus the laser beam on points on the surface where the secondary phases are located. For all these reasons, the samples were analyzed in Catalonia Institute for Energy Research

(IREC) using Raman spectroscopy with different lasers with excitation wavelength  $\lambda = 325$  nm and  $\lambda = 532$  nm with spot size of about 70  $\mu\text{m}$ . These measurement conditions are more sensitive to specific secondary phases and are capable to inspect larger areas confirming the presence of ZnS as well as SnS<sub>2</sub> (see Figure 3.8).

The Raman spectra of the post-annealed CZTS powder crystals measured with excitation wavelength  $\lambda = 325$  nm revealed the presence of ZnS secondary phase with Raman peaks centered at 348, 697 and 1045  $\text{cm}^{-1}$  (see Figure 3.8 left) [75]. The Raman spectra of the post-annealed CZTS powder crystals measured with excitation wavelength  $\lambda = 532$  nm exhibited an intense peak centered at 314  $\text{cm}^{-1}$  in addition to the peaks corresponding to the kesterite CZTS phase (see Figure 3.8 right). According to the literature data, this peak belongs to the SnS<sub>2</sub> secondary phase [76]

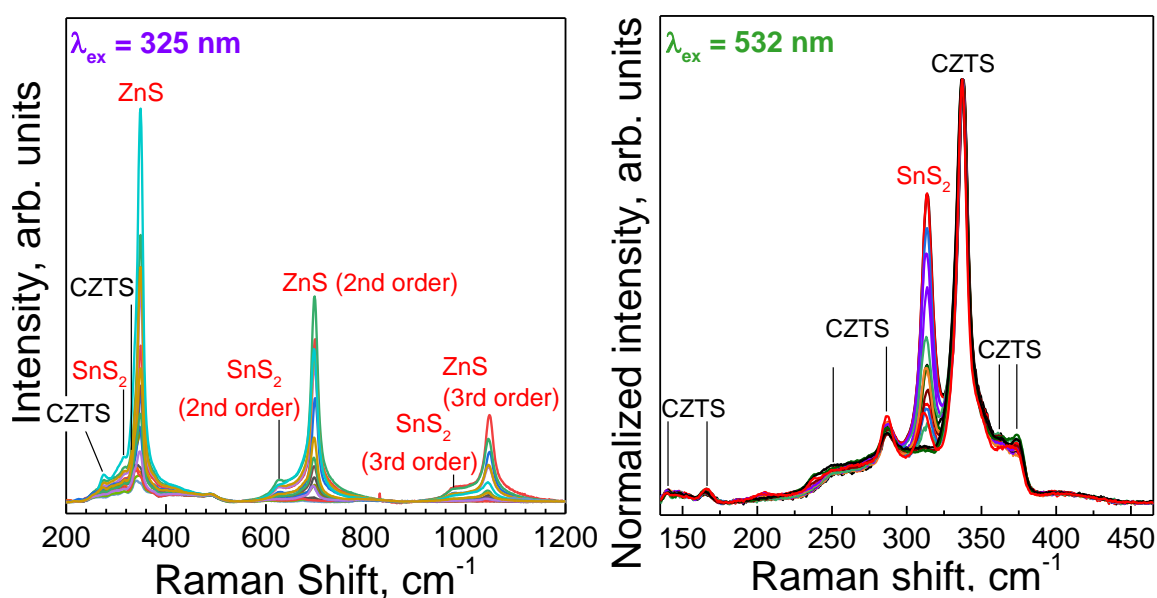


Figure 3.6 Raman spectra of CZTS monograin powder crystals annealed at different regimes in sulfur atmosphere and analyzed at (left) 325 nm and (right) 532 nm laser wavelengths

### 3.1.3 Bulk composition of CZTS monograins after post-annealing in sulfur atmosphere

Bulk and surface composition of as-grown Cu<sub>2</sub>ZnSnS<sub>4</sub> monograins have been characterized by EDX. In Figure 3.9 EDX images of the cross-section and surface of CZTS crystals can be seen. In Figure 3.9a, the light grey regions correspond to CZTS material while the darker and smaller regions inside the monograins belong to the ZnS secondary phase.

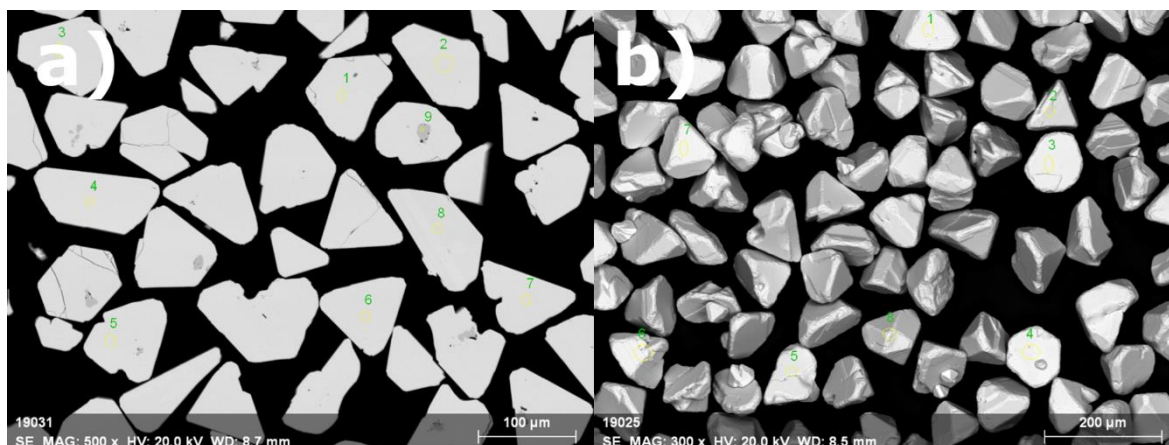


Figure 3.7 SEM images of a) polished cross-section of as-grown CZTS crystals' bulk and b) surface of the CZTS monograins

The average composition of as-grown CZTS powder was calculated from the EDX measurements of the cross-section of 8 different grains. Additionally, the composition of grain number 9 in Figure 3.9a corresponds to ZnS. The average elemental composition of CZTS (at.%) is shown in Table 3.2 for both bulk and surface.

Table 3.2 Elemental composition of  $\text{Cu}_2\text{ZnSnS}_4$  as-grown monograin powder crystals' bulk and surface

	<b>Cu, at.%</b>	<b>Zn, at.%</b>	<b>Sn, at.%</b>	<b>S, at.%</b>
Bulk	23.5	13.8	12.6	50.0
Surface	23.8	13.7	12.6	49.8

The chemical composition of bulk and surface slightly differs being surface Cu richer than in the bulk.

In the following graphs (Figure 3.10), the average compositional ratios of CZTS powders as-grown and after annealing at different temperatures and sulfur vapor pressures is shown.

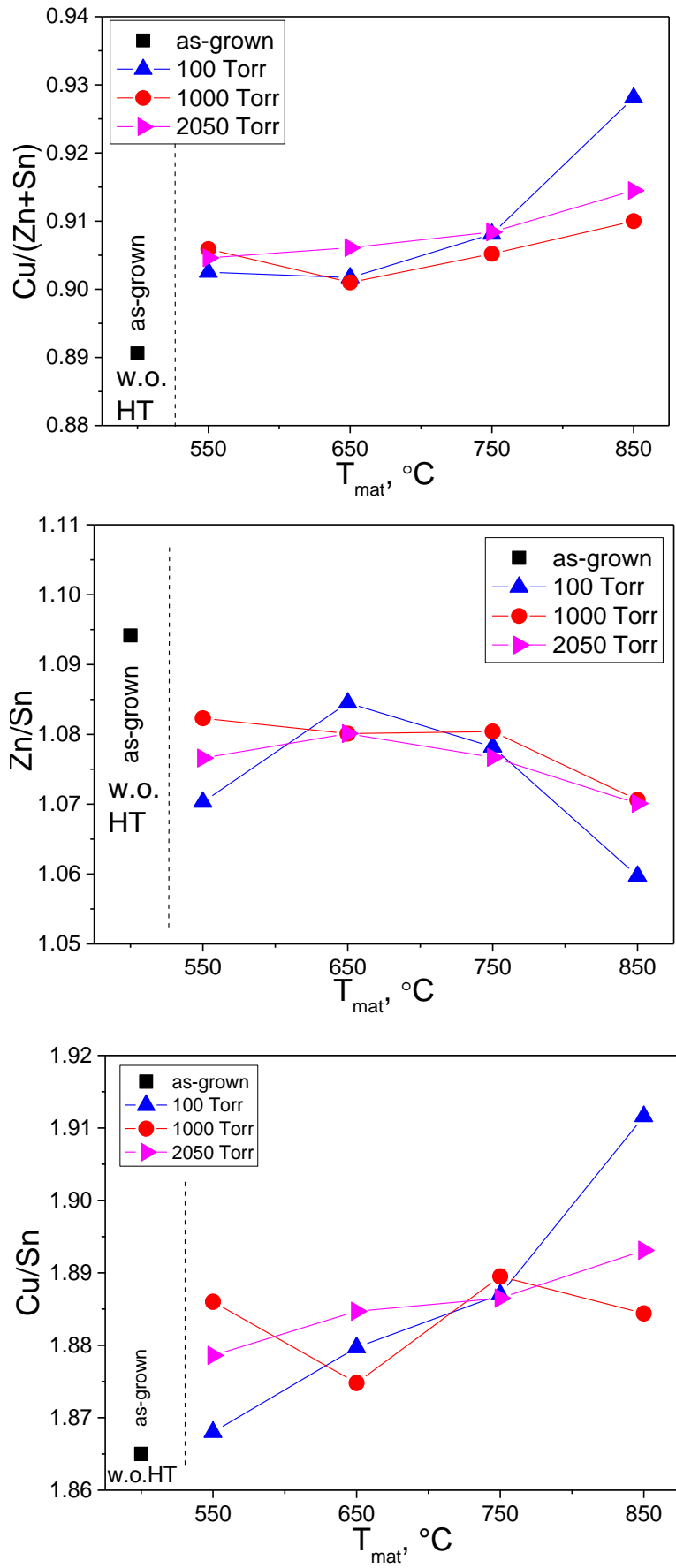


Figure 3.8 The changes in compositional ratio of Cu/(Zn+Sn), Zn/Sn and Cu/Sn in CZTS monograin powder crystals depending on the post-annealing regime as determined by EDX

The concentration of copper in crystals' bulk increases with the increase in annealing temperature of CZTS. The ratio of  $[Cu]/([Zn]+[Sn])$  and  $[Cu]/[Sn]$  is seen to be increased when increasing the temperature for all the different vapor pressures used. Cu concentration is also higher compared to the as-grown monograins. The compositional ratio of  $Cu/(Zn+Sn)$  increased from 0.89 to 0.93 (Figure 3.10a) by increasing the annealing temperature from 550 to 850 °C, and the ratio of Zn/Sn decreased from 1.09 to 1.06 (Figure 3.10b) in the bulk of CZTS crystals compared to as-grown monograin powder crystals. The highest values of Cu concentration have been found at low sulfur vapor pressure (100 Torr) and high annealing temperature (850 °C). In all cases it is seen that Cu diffuses into the material after annealing. As Zn tends to diffuse towards the surface, Zn-rich secondary phases are therefore expected on the crystals' surfaces.

The obtained findings are in good agreement with the results reported by J. Zhong *et al.* [61]. They found experimentally and presented the schematic elemental diffusion routes and surface reaction mechanism during the sulfurization of CZTSSe (see Figure 1.7). As a result, the high Cu diffusion ability toward Mo layer and Zn and Sn diffusion toward surface of the CZTSSe forming Cu-poor surface was demonstrated. On the surface, the reaction of Zn and Sn with sulfur was proposed to form ZnS, SnS(Se) and SnS(Se)<sub>2</sub>.

### 3.1.4 Characterization of the CZTS monograin layer solar cells

Table 3.3 and 3.4 summarizes the results of the characterization of 24 monograin layer solar cells in dependence of varied post-annealing regime in sulfur atmosphere. For each solar cell, only the best performance from the 6 different areas measured is shown.

Table 3.1 Characteristic parameters of CZTS monograin layer solar cells depending on absorber powder post-annealing temperatures and applied sulfur vapor pressures after annealing for 20 minutes

$T_{mat}$ , °C	$P_s$ , Torr	$V_{oc}$ , mV	$J_{sc}$ , mA/cm <sup>2</sup>	$FF$ , %	$\eta_{active}$ , %
550	100	708	15.2	52.2	5.60
550	1000	725	15.5	58.0	6.53
550	2050	689	17.0	48.8	5.72
650	100	720	15.5	56.2	6.23
650	1000	732	15.0	54.7	6.00
650	2050	725	15.5	54.5	6.12
750	100	733	14.8	55.7	5.94
750	1000	715	15.5	56.9	6.28
750	2050	720	15.6	51.0	5.71
850	100	667	15.9	53.5	5.66
850	1000	710	15.6	55.4	6.11
850	2050	714	15.8	54.6	6.17

Table 3.2 Characteristic parameters of CZTS monograin layer solar cells depending on absorber powder post-annealing temperatures and applied sulfur vapor pressures after annealing for 60 minutes

$T_{mat}$ , °C	$P_{S}$ , Torr	$V_{oc}$ , mV	$J_{sc}$ , mA/cm <sup>2</sup>	$FF$ , %	$\eta_{active}$ , %
550	100	735	15.7	53.0	6.10
550	1000	740	13.9	59.8	6.15
550	2047	725	15.9	55.7	6.42
650	100	735	15.9	52.9	6.19
650	1000	737	14.6	54.4	5.84
650	2047	734	15.7	55.2	6.22
750	100	722	15.4	51.4	5.69
750	1000	729	15.0	55.7	6.09
750	2047	716	14.6	57.6	6.02
850	100	677	14.5	50.0	4.91
850	1000	709	15.9	56.1	6.33
850	2047	715	15.6	58.8	6.56

The increasing of annealing time leads to a higher open circuit voltage in material temperatures at 550 and 650 °C, but not in the case of material temperatures at 750 and 850 °C (achieved values were at the same level).

Characteristic parameters of CZTS monograin layer solar cells depending on absorber powder post-annealing temperatures and applied sulfur vapor pressures (annealed for 60 minutes) are illustrated also in Figure 3.11. Compared to the parameters of solar cell based on unannealed absorber material, almost all monograin layer solar cell parameters improved remarkably after post-annealing in sulfur atmosphere. The highest  $V_{oc}$  of 740 and fill factor of ~60% values were achieved by solar cell based on powder annealed at  $T_{mat} = 550$  °C under  $P_s = 1000$  Torr for 60 minutes (Figure 3.11a and b). From the Tables 3.3 and 3.4 and Figure 3.11 it can be seen that a vapor pressure of 100 torr was not enough for a  $T_{mat}$  of 850 °C and the solar cell parameters started to decrease. Applied vapor pressure was too low to avoid the decomposition of CZTS compound. This effect was more visible when the sample remained 60 minutes under this temperature.

All annealed samples gave a better performance than the as-grown one and the experimental results confirmed that it is always necessary to etch and anneal the CZTS monograin powders [37]. Optimal condition for post-treatment to improve MGL solar cells` performance was found to involve annealing in sealed ampoules at 850 °C in a sulfur atmosphere of 2050 Torr for 1 hour to adjust the absorber material composition. The highest conversion efficiency of 6.56% was obtained under these conditions.

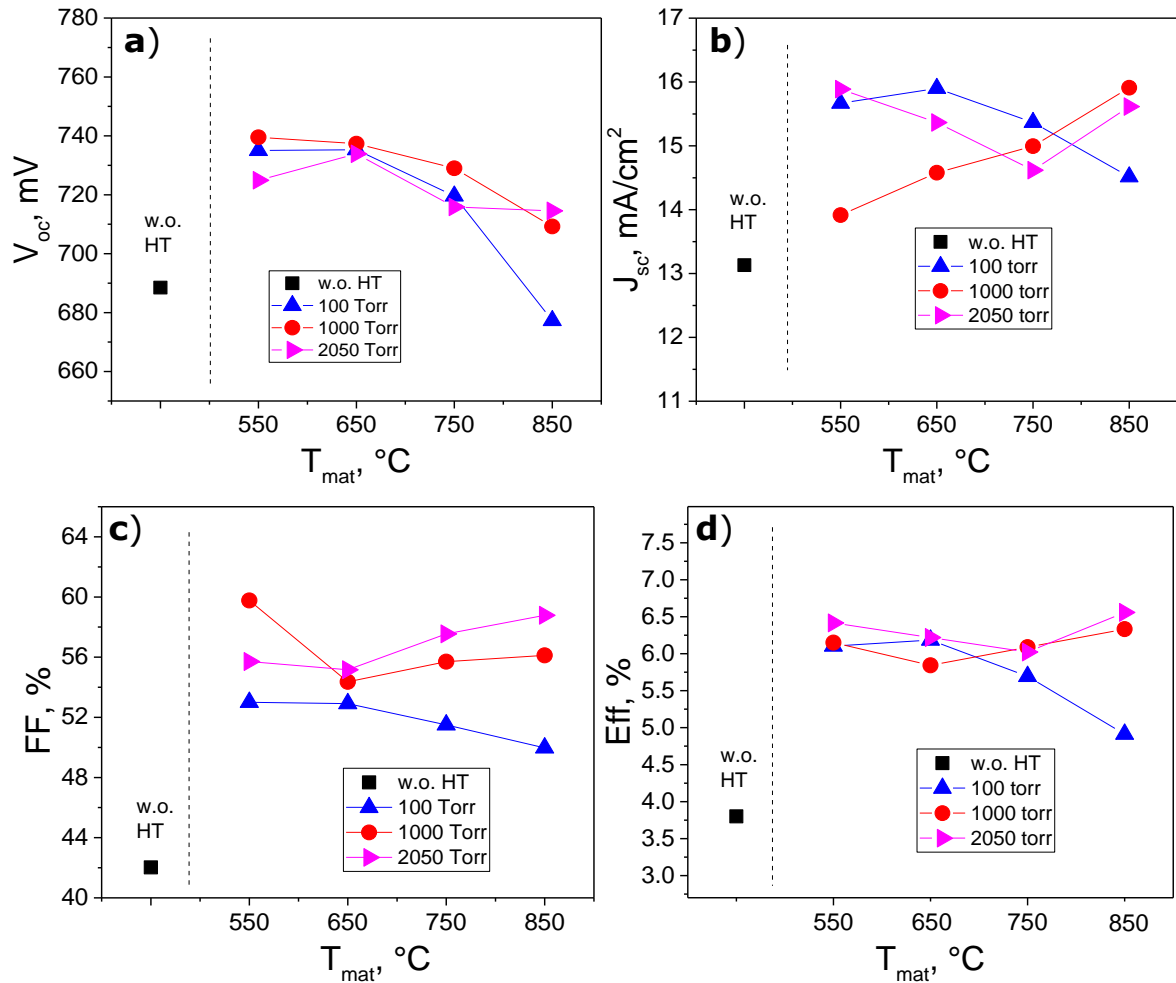


Figure 3.9 a) open-circuit voltage, b) current density, c) fill factor and d) efficiency of CZTS monograin layer solar cells in dependence of used post-annealing conditions of T<sub>mat</sub> and P<sub>s</sub> (annealed for 60 minutes)

The evaluation of band gap energy ( $E_g$ ) from the optical absorption or reflectance spectra of the monograin powders is rather challenging. Instead, the effective band gap energy ( $E_g^*$ ) can be estimated using the external quantum efficiency analysis of the synthesized powders. The EQE of Cu<sub>2</sub>ZnSnS<sub>4</sub> MGL solar cells was measured as a function of the incident light wavelength at room temperature.  $E_g^*$  can be estimated from the linear segment of the low-energy side of  $(E^*QE)^2$  vs.  $E$  curves [77] (Figure 3.12a).

The effective band gap energy values of different powders at different annealing conditions has been calculated (Figure 3.12b) and most of the values are seen to remain practically constant between  $E_g^* = 1.55 - 1.57$  eV. A slight shift to the lower values can be seen with the effective band gap energy values at 850 °C ( $E_g^* = 1.54$  eV).

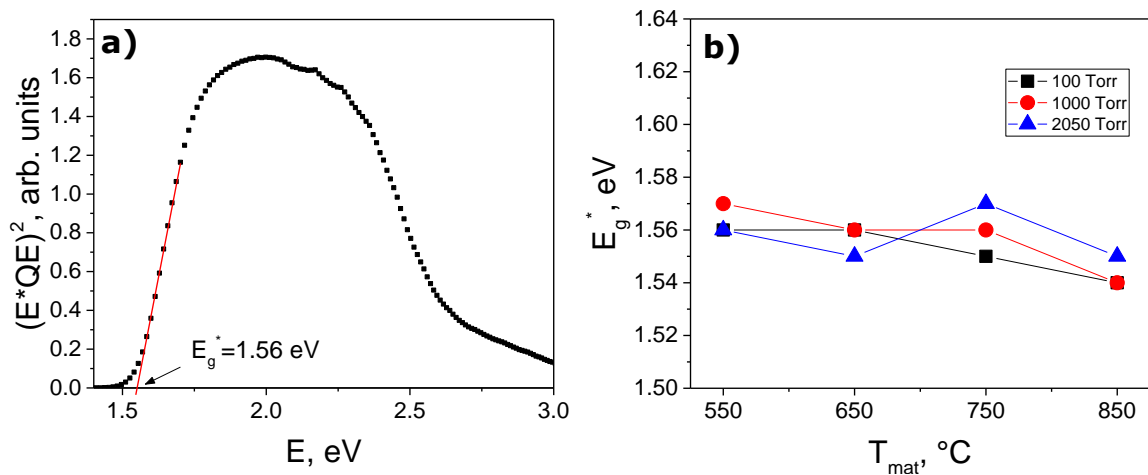


Figure 3.10 a) Determination of CZTS band gap energy values from EQE data of MGL solar cells based on MGP annealed at  $T_{mat} = 850$  °C and  $T_s = 550$  °C; b) Effective band gap energy values of CZTS monograin powders in dependence of used post-annealing conditions of  $T_{mat}$  and  $P_s$  (annealed for 60 minutes)

### 3.2 Post annealing in sulfur and argon atmosphere

According to the results of SEM, EDX and Raman analysis, all powders contained some crystals, which were covered with ZnS and/or SnS<sub>2</sub> after post-annealing in sulfur atmosphere, independent of applied conditions. Moreover, the detected amounts of ZnS and SnS<sub>2</sub> were not dependent on applied post-annealing regime. However, only SnS<sub>2</sub> of layered structure had formed on large areas at the surface of CZTS crystals during post-annealing process under different sulfur pressures.

Several reports have shown [54][49][48] that SnS<sub>2</sub> forms on the crystals' surfaces during sulfur treatment and decreases the solar cell parameters. M. Kumar *et al.* [48] reported that SnS<sub>2</sub> is a *n*-type semiconductor with a band gap of 2.2 eV. This may form a secondary diode inside the absorbing layer, or it could be insulating in nature, which can cause high photocarrier recombination.

Therefore, the post-annealed CZTS monograin powder crystals were studied also after CdS deposition process by SEM (see Figure 3.14). CdS buffer layer was deposited by chemical bath deposition method. It can be seen that CdS is not being deposited homogeneously on SnS<sub>2</sub> secondary phase areas. Also, Figure 3.14b, c and d show that some layers of SnS<sub>2</sub> have been dissolved during the CBD process. In this case, CdS is neither being deposited homogeneously on the areas left by SnS<sub>2</sub>.

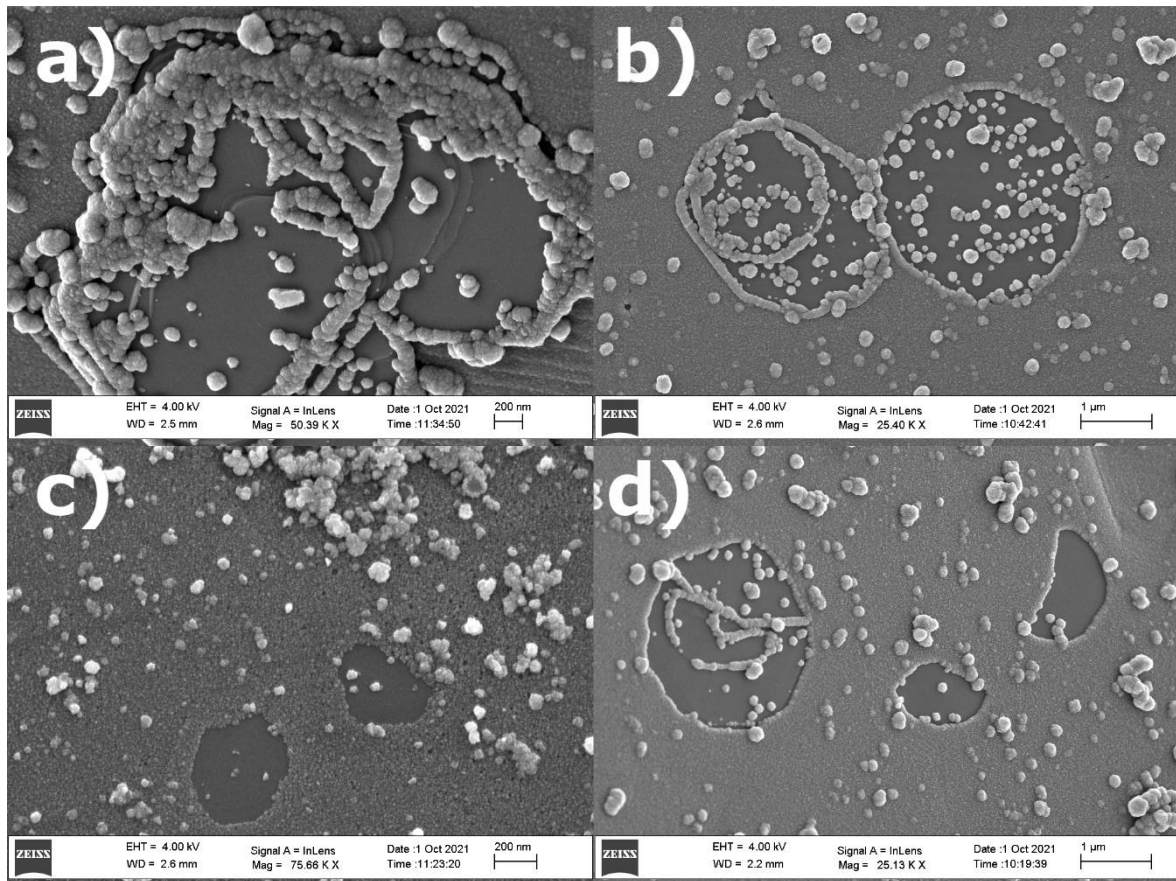


Figure 3.14 SEM images of the post-annealed CZTS monograin powder crystals' surfaces ( $\text{SnS}_2$  covered areas) after the CdS deposition

The characterization of MGL solar cell by electron beam-induced current (EBIC) (Figure 3.15b and d) confirmed that  $\text{SnS}_2$  destroys the  $p$ - $n$  junction, these areas (seen as darker spots on CZTS crystal surface in Figure 3.15b and d) are less-functional and are therefore detrimental to the performance of CZTS device. Thus,  $\text{SnS}_2$  secondary phases have to be removed before the deposition of CdS to improve the final performance of the MGL solar cells.

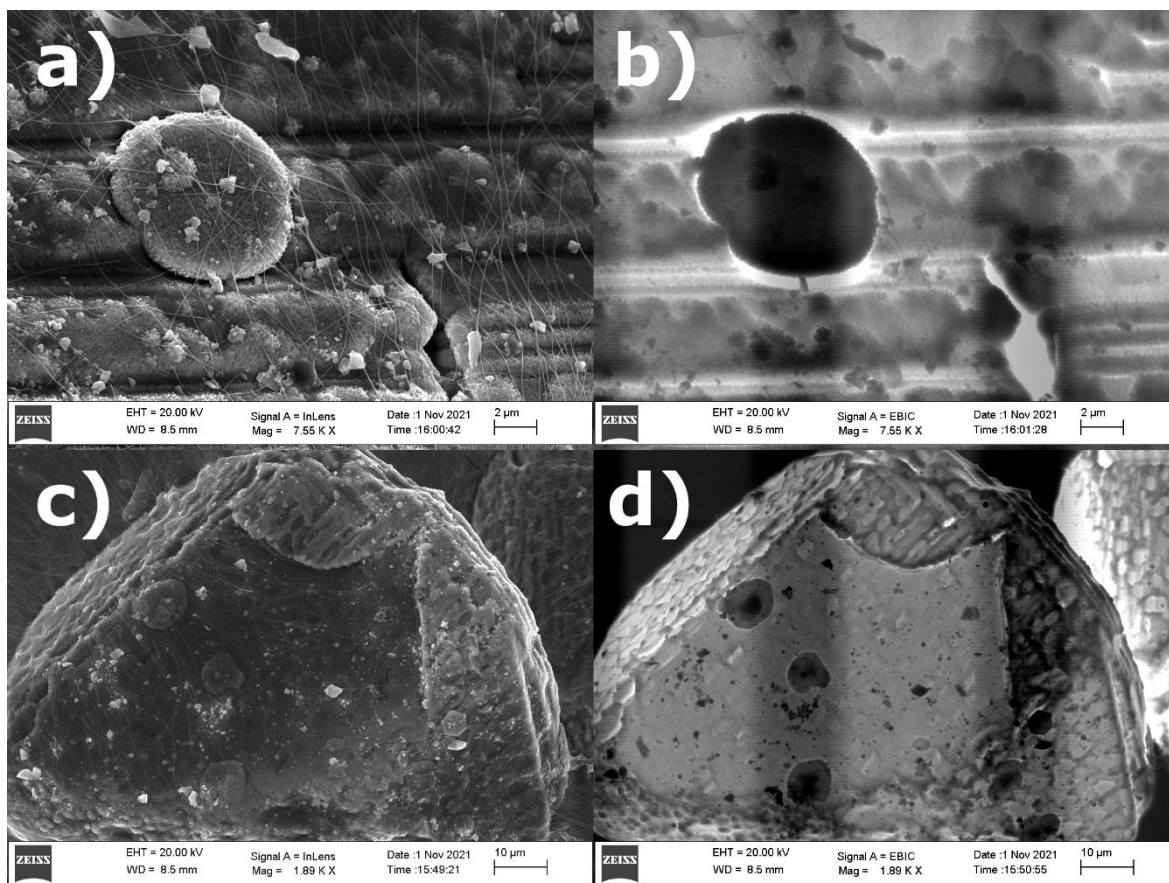


Figure 3.15 SEM (a-c) and EBIC (b-d) images of a post-treated and CdS covered CZTS monograin powder crystals

To try to avoid the formation and/or precipitation of the SnS<sub>2</sub> secondary phase on MGP crystals' surfaces, inert argon gas was added to the sulfur atmosphere. Monograins were etched in the standard way and annealed in sulfur plus argon atmospheres. The same amount of sulfur was used in all the cases, the post-annealing temperature was kept on material side at 850 °C and on sulfur side at 550 °C. Annealing time was 60 minutes. Four different argon pressures were added to the post-annealing ampoules (10, 50, 100 and 300 Torr).

### 3.2.1 Elemental composition of CZTS monograin powders post-annealed in sulfur and argon atmosphere

Bulk composition of Cu<sub>2</sub>ZnSnS<sub>4</sub> monograins annealed in sulfur and argon atmosphere have been characterized by EDX. In Figure 3.16 SEM images of the cross-section of CZTS can be seen, the light regions (in grains 1 - 8) correspond to CZTS material while the darker and smaller region (area number 9) inside the monograin belongs to the ZnS

secondary phase. Based on EDX analysis, ZnS as secondary phase has been found in all the powders annealed under different argon pressure regimes.

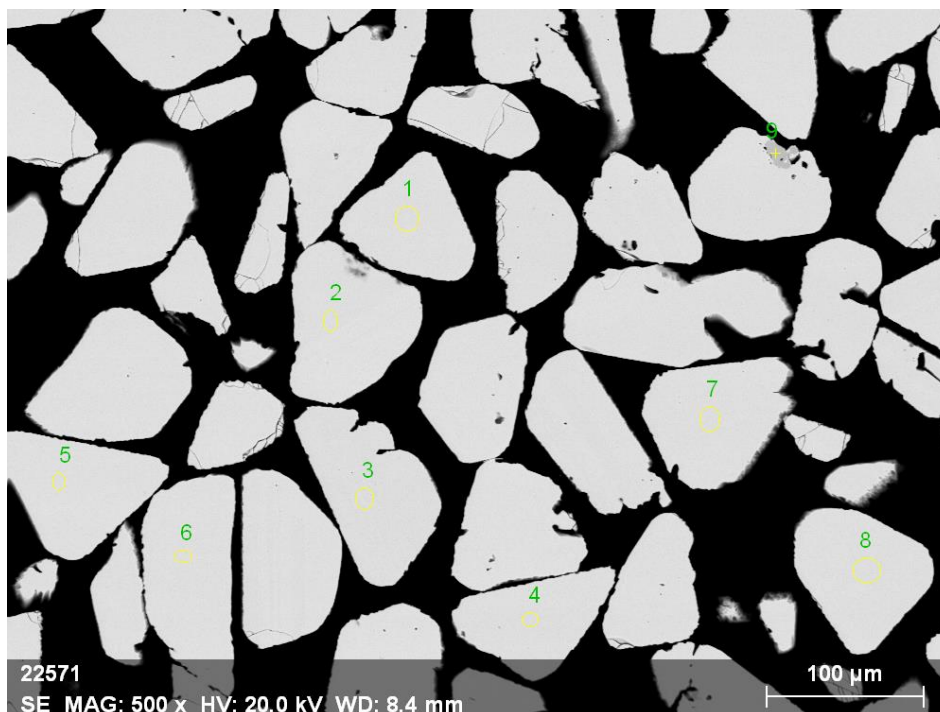


Figure 3.16 SEM image of polished cross-section of CZTS monograin powder crystals` post-annealed under sulfur and argon atmosphere

Table 3.5 Elemental composition of CZTS monograin powders annealed under sulfur and different argon pressures

$P_{Ar}$ , Torr	Cu, at.%	Zn, at.%	Sn, at.%	S, at.%
0	23.90	13.50	12.57	50.03
10	23.90	13.42	12.63	50.05
50	23.87	13.51	12.60	50.03
100	24.00	13.46	12.57	49.97
300	23.89	13.50	13.57	50.05

In Figure 3.17, the elemental composition of CZTS monograin powders annealed at different argon vapor pressures is shown. Only tin concentration is slightly higher at 300 Torr than in all the other regimes. The concentration of the other elements (Cu, Zn, and S) remained constant independently of the argon vapor pressure used.

The ratio of metals  $[Cu]/([Zn]+[Sn]) = 0.93$ ,  $[Cu]/[Sn] = 1.90$  and  $[Zn]/[Sn] = 1.07$  also stayed constant for all annealed powders except for powder annealed at 300 Torr, where the values were lower as the concentration of Sn in this case was higher. The ratios were  $[Cu]/([Zn]+[Sn]) = 0.88$ ,  $[Cu]/[Sn] = 1.76$  and  $[Zn]/[Sn] = 1.00$ .

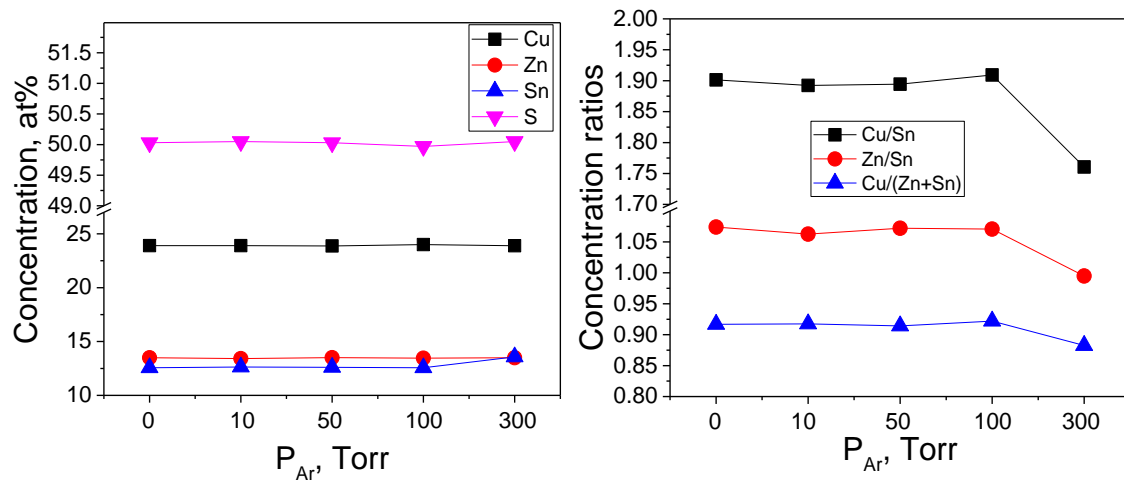


Figure 3.11 Concentration of Cu, Sn, Zn and S (left); and concentration ratios of [Cu]/[Sn], [Zn]/[Sn] and [Cu]/([Zn]+[Sn]) in CZTS MGPs after annealing under different Argon pressures (right)

### 3.2.2 Morphology of CZTS monograin powders post-annealed in sulfur and argon atmosphere

SEM images of CZTS MGP crystals after post-annealing under argon pressures of 10, 50, 100 and 300 Torr are presented in Figure 3.18. Crystals' surfaces of monograin powders annealed in argon atmosphere are rougher than as-grown powders as well as sulfur treated ones. In all different samples, SnS<sub>2</sub> layers (darker areas in Figure 3.18) are still presented on the surface of the crystals. The detected amount of SnS<sub>2</sub> was not dependent on applied argon pressure.

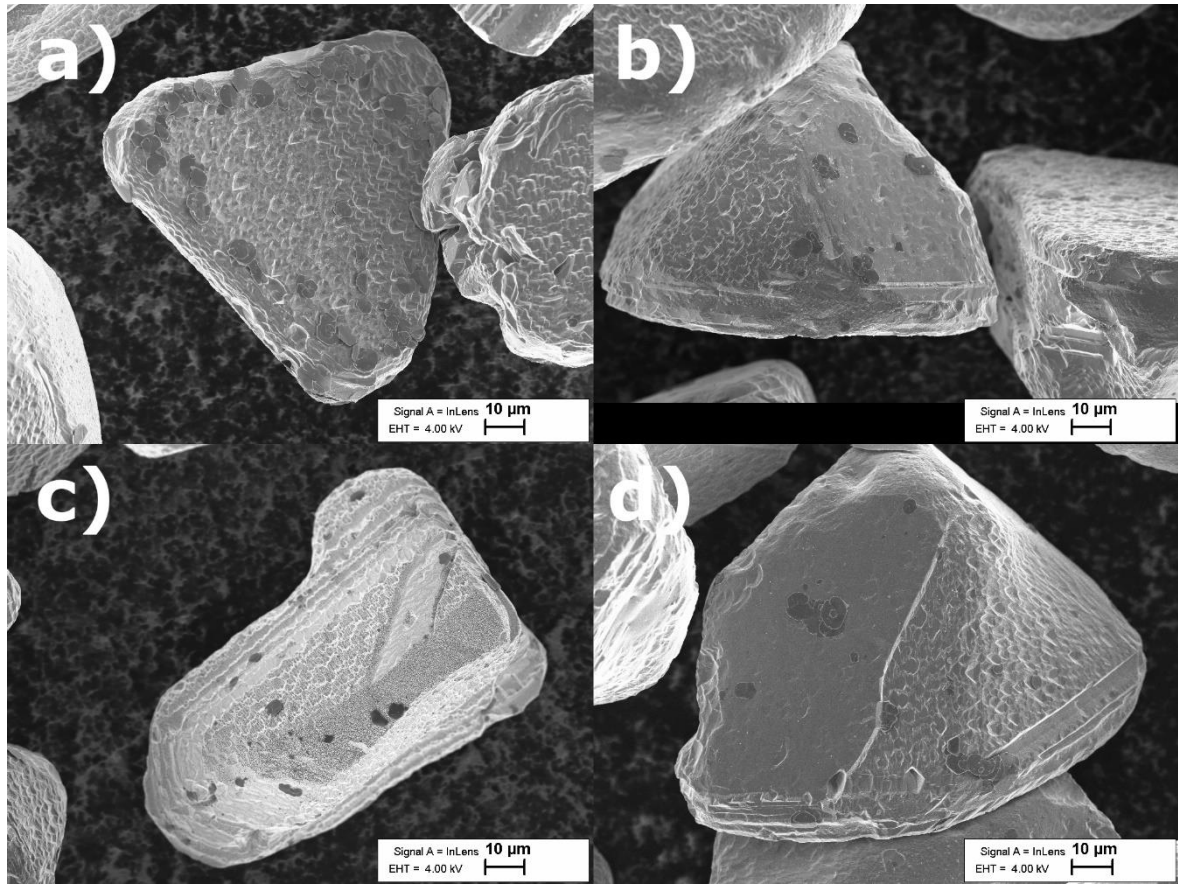


Figure 3.12 SEM images of the CZTS monograin powders etched and annealed under different argon pressures in sulfur atmosphere

### 3.2.3 Characterization of the MGL solar cells based on CZTS monograin powders annealed in sulfur and argon atmosphere

In Table 3.9, the results of the characterization of 5 monograin layer solar cells in different post-annealing regime in sulfur and argon atmosphere are shown. For each solar cell, only the best performance from the grid of gold contacts measured is depicted.

Table 3.3 Main parameters of the solar cells annealed in an argon atmosphere at different pressures

$P_{Ar}$ , Torr	$V_{oc}$ , mV	$J_{sc}$ , mA/cm <sup>2</sup>	FF, %	$\eta_{active}$ , %
0	717	17.4	67.6	8.42
10	706	15.5	64.2	7.02
50	691	15.2	62.4	6.56
100	658	15.1	58.6	5.80
300	688	17.5	59.4	7.16

From the characterized solar cells, it cannot be seen any improvement in terms of efficiency for the different argon pressures used, if to compare with the solar cell based on the CZTS powder annealed in a sulfur atmosphere without additional argon pressure. This solar cell gave the best performance ( $\eta_{\text{active}} = 8.42\%$ ) followed by the one ( $\eta_{\text{active}} = 7.16\%$ ) with the highest argon vapor pressure of  $P_{\text{Ar}} = 300$  Torr (Figure 3.19).

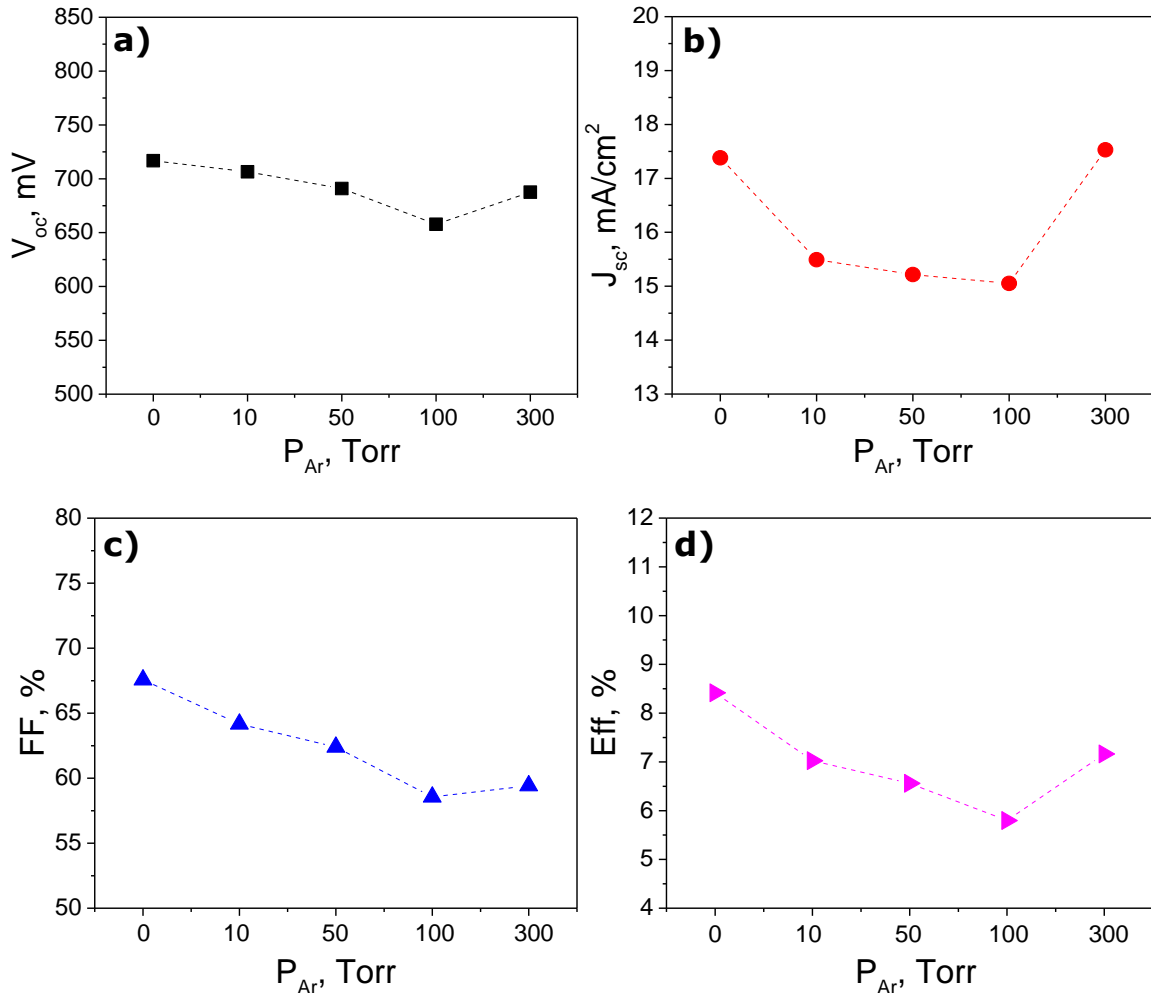


Figure 3.13 a) open-circuit voltage, b) current density, c) fill factor and d) efficiency of CZTS monograin layer solar cells in dependence of used argon pressures during post-annealing in sulfur atmosphere at  $T_{\text{mat}} = 850$  °C and  $T_{\text{s}} = 550$  °C

To sum up, the presence of argon inside the ampoule during the annealing process did not help in avoiding the formation of  $\text{SnS}_2$  and the performance of the MGL solar cells was not better than without the additional pressure of the inert gas. Only the solar cell treated under the highest argon pressure (300 Torr) showed a slightly better current density value than the one annealed only in sulfur atmosphere. For all the other solar cells conversion efficiency, open circuit voltage and fill factor values were lower and the trend was negative for the different argon pressures. As a result, the effect of additional

argon pressure during the post-annealing process was the opposite of the expected: the precipitation of SnS<sub>2</sub> was not inhibited; even worse, the parameters of solar cells decreased. Further studies are required to find methods for removing the SnS<sub>2</sub> secondary phase from the surfaces of MPG crystals after the post-annealing process and before CdS deposition.

## SUMMARY

The main objective of this thesis was to investigate the effect of different post-annealing conditions in sulfur atmosphere on the crystals' surface and bulk composition of  $\text{Cu}_2\text{ZnSnS}_4$  monograin powders, and to prepare and characterize monograin layer solar cells based on these materials.

$\text{Cu}_2\text{ZnSnS}_4$  monograin powders used in this study were synthesized in vacuumed quartz ampoules from high purity (99.999%) binary precursors CuS, SnS and ZnS in the liquid phase of KI (99.99%). The chemically etched monograin powders were annealed at different temperatures (550, 650, 750 and 850 °C) under different sulfur vapor pressures (100, 1000, 2050 Torr) in a two-zone furnace in closed ampoules. In addition a series of experiments were performed by adding inert argon gas to the sulfur. Four different pressures of argon were used (10, 50, 100, and 300 Torr). MGL solar cells were prepared from the different powders having a superstrate structure of graphite(gold)/CZTS/CdS/i-ZnO/ZnO:Al/Ag/glass.

- According to EDX analysis, by increasing the annealing temperature from 550 to 850 °C, the ratio of Cu/(Zn+Sn) and Cu/Sn increased, and Zn/Sn decreased in the bulk of annealed CZTS crystals compared to as-grown MGP crystals. Concentration ratios of the different elements of sulfur plus argon treated monograin powders remained constant except for the highest argon pressure (300 Torr) where a slightly higher tin content was found.
- EDX elemental mapping and Raman studies showed that large-size  $\text{SnS}_2$  layers and ZnS secondary phases were formed on the crystals' surfaces in the thermal annealing process.
- SEM images of CZTS MGPs after post-annealing at different regimes revealed the presence of  $\text{SnS}_2$  secondary phase on crystals' surfaces for all used conditions and for both atmospheres (sulfur and sulfur plus argon).
- EBIC analysis confirmed, that the formation of large-size  $\text{SnS}_2$  layers on MGP crystals' surfaces in the thermal annealing process is detrimental for MGL solar cells performance (these areas are less-functional).
- EQE analysis showed that the band gap energy of MGL solar cells did not change significantly for the different temperatures and sulfur pressures and was  $\sim 1.56$  eV.
- *I-V* characteristics of MGL solar cells showed remarkable improvement after post-annealings in sulfur atmosphere compared to the parameters of solar cell based on un-annealed absorber material. The presence of argon pressure during the

annealing process in sulfur atmosphere had detrimental effect for solar cell parameters. Only the solar cell treated under 300 Torr argon pressure showed a slightly better current density value than the one annealed only under sulfur pressure.

- The MGL solar cell annealed at 850 °C in a 2050 Torr sulfur atmosphere for 1 hour exhibited the highest power conversion efficiency of 8.42% (active area), with an open-circuit voltage of 717 mV, current density of 17.4 mA/cm<sup>2</sup> and a fill factor of 67.6% using gold contacts.

Future research is needed to find methods to remove or to avoid the formation of SnS<sub>2</sub> secondary phase on the surfaces of MPG crystals through different thermal treatments or chemical etchings.

## LIST OF REFERENCES

- [1] 2030 Climate & Energy Framework, (n.d.). [https://ec.europa.eu/clima/eu-action/climate-strategies-targets/2030-climate-energy-framework\\_en](https://ec.europa.eu/clima/eu-action/climate-strategies-targets/2030-climate-energy-framework_en) (accessed April 21, 2022).
- [2] A. Muratoglu, M.I. Yuce, World Energy Outlook and Place of Renewable Resources, *Int. J. Sci. Technol. Res. Wwww.Iiste.Org* ISSN. 1 (2015). [www.iiste.org](http://www.iiste.org).
- [3] Irena, Renewable Power Generation Costs in 2020, (2021). <https://www.irena.org/publications/2021/Jun/Renewable-Power-Costs-in-2020>.
- [4] J. Zhou, X. Xu, B. Duan, H. Wu, J. Shi, Y. Luo, D. Li, Q. Meng, Regulating crystal growth via organic lithium salt additive for efficient Kesterite solar cells, *Nano Energy*. 89 (2021) 106405. <https://doi.org/10.1016/j.nanoen.2021.106405>.
- [5] Y. Gong, Y. Zhang, Q. Zhu, Y. Zhou, R. Qiu, C. Niu, W. Yan, W. Huang, H. Xin, Identifying the origin of the: V ocdeficit of kesterite solar cells from the two grain growth mechanisms induced by Sn<sup>2+</sup>and Sn<sup>4+</sup>precursors in DMSO solution, *Energy Environ. Sci.* 14 (2021) 2369–2380. <https://doi.org/10.1039/d0ee03702h>.
- [6] H.S. Nugroho, G. Refantero, N.L.W. Septiani, M. Iqbal, S. Marno, H. Abdullah, E.C. Prima, Nugraha, B. Yuliarto, A progress review on the modification of CZTS(e)-based thin-film solar cells, *J. Ind. Eng. Chem.* 105 (2022) 83–110. <https://doi.org/https://doi.org/10.1016/j.jiec.2021.09.010>.
- [7] K. Pal, P. Singh, A. Bhaduri, K.B. Thapa, Current challenges and future prospects for a highly efficient (>20%) kesterite CZTS solar cell: A review, *Sol. Energy Mater. Sol. Cells*. 196 (2019) 138–156. <https://doi.org/10.1016/j.solmat.2019.03.001>.
- [8] R.A. Marques Lameirinhas, J.P.N. Torres, J.P. de Melo Cunha, A Photovoltaic Technology Review: History, Fundamentals and Applications, *Energies*. 15 (2022) 1–44. <https://doi.org/10.3390/en15051823>.
- [9] D.M. Chapin, C.S. Fuller, G.L. Pearson, A new silicon p-n junction photocell for converting solar radiation into electrical power, *J. Appl. Phys.* 25 (1954) 676–677. <https://doi.org/10.1063/1.1721711>.

- [10] M.H. Boratto, Semiconducting and Insulating oxides applied to electronic devices, (2018) 1–118.
- [11] C.B.H. and S.G.Bowden, Photovoltaics Education Website, (2019). <https://www.pveducation.org/> (accessed April 21, 2022).
- [12] O.K. Simya, P. Radhakrishnan, A. Ashok, K. Kavitha, R. Althaf, Engineered nanomaterials for energy applications, *Handb. Nanomater. Ind. Appl.* (2018) 751–767. <https://doi.org/10.1016/B978-0-12-813351-4.00043-2>.
- [13] A. Mandong, Design and simulation of single , double and multy-layer Faculty of Engineering Master ' s Thesis, (2019). <https://doi.org/10.13140/RG.2.2.23475.58408>.
- [14] A. Belghachi, Theoretical Calculation of the Efficiency Limit for Solar Cells, *Sol. Cells - New Approaches Rev.* (2015). <https://doi.org/10.5772/58914>.
- [15] F.L. Curzon, B. Ahlborn, Efficiency of a Carnot engine at maximum power output, *Am. J. Phys.* 43 (1975) 22–24. <https://doi.org/10.1119/1.10023>.
- [16] M.I. Hossain, W. Qarony, S. Ma, L. Zeng, D. Knipp, Y.H. Tsang, Perovskite/Silicon Tandem Solar Cells: From Detailed Balance Limit Calculations to Photon Management, *Nano-Micro Lett.* 11 (2019) 1–24. <https://doi.org/10.1007/s40820-019-0287-8>.
- [17] E. Radziemska, The effect of temperature on the power drop in crystalline silicon solar cells, *Renew. Energy.* 28 (2003) 1–12. [https://doi.org/10.1016/S0960-1481\(02\)00015-0](https://doi.org/10.1016/S0960-1481(02)00015-0).
- [18] P. Singh, S.N. Singh, M. Lal, M. Husain, Temperature dependence of I-V characteristics and performance parameters of silicon solar cell, *Sol. Energy Mater. Sol. Cells.* 92 (2008) 1611–1616. <https://doi.org/10.1016/j.solmat.2008.07.010>.
- [19] P.G.V. Sampaio, M.O.A. González, Photovoltaic solar energy: Conceptual framework, *Renew. Sustain. Energy Rev.* 74 (2017) 590–601. <https://doi.org/10.1016/j.rser.2017.02.081>.
- [20] C. Battaglia, A. Cuevas, S. De Wolf, High-efficiency crystalline silicon solar cells: Status and perspectives, *Energy Environ. Sci.* 9 (2016) 1552–1576. <https://doi.org/10.1039/c5ee03380b>.

- [21] B. Rech, H. Wagner, Potential of amorphous silicon for solar cells, *Appl. Phys. A Mater. Sci. Process.* 69 (1999) 155–167.  
<https://doi.org/10.1007/s003390050986>.
- [22] M.A. Green, E.D. Dunlop, J. Hohl-Ebinger, M. Yoshita, N. Kopidakis, X. Hao, Solar cell efficiency tables (version 56), *Prog. Photovoltaics Res. Appl.* 28 (2020) 629–638. <https://doi.org/10.1002/pip.3303>.
- [23] M. Nakamura, K. Yamaguchi, Y. Kimoto, Y. Yasaki, T. Kato, H. Sugimoto, Cd-Free Cu (In, Ga)(Se, S)<sub>2</sub> Thin-Film Solar Cell With Record Efficiency of 23.35 %, *Ieee.* 9 (2019) 1863–1867.
- [24] L. Hong, H. Yao, Y. Cui, P. Bi, T. Zhang, Y. Cheng, Y. Zu, J. Qin, R. Yu, Z. Ge, J. Hou, 18.5% Efficiency Organic Solar Cells with a Hybrid Planar/Bulk Heterojunction, *Adv. Mater.* 33 (2021).  
<https://doi.org/10.1002/adma.202103091>.
- [25] Y. Cao, Y. Liu, S.M. Zakeeruddin, A. Hagfeldt, M. Grätzel, Direct Contact of Selective Charge Extraction Layers Enables High-Efficiency Molecular Photovoltaics, *Joule.* 2 (2018) 1108–1117.  
<https://doi.org/10.1016/j.joule.2018.03.017>.
- [26] W. Wang, M.T. Winkler, O. Gunawan, T. Gokmen, T.K. Todorov, Y. Zhu, D.B. Mitzi, Device characteristics of CZTSSe thin-film solar cells with 12.6% efficiency, *Adv. Energy Mater.* 4 (2014) 1–5.  
<https://doi.org/10.1002/aenm.201301465>.
- [27] W. Chen, Y. Zhu, J. Xiu, G. Chen, H. Liang, S. Liu, H. Xue, E. Birgersson, J.W. Ho, X. Qin, J. Lin, R. Ma, T. Liu, Y. He, A.M.C. Ng, X. Guo, Z. He, H. Yan, A.B. Djurišić, Y. Hou, Monolithic perovskite/organic tandem solar cells with 23.6% efficiency enabled by reduced voltage losses and optimized interconnecting layer, *Nat. Energy.* 7 (2022) 229–237. <https://doi.org/10.1038/s41560-021-00966-8>.
- [28] M. Hao, Y. Bai, S. Zeiske, L. Ren, J. Liu, Y. Yuan, N. Zarrabi, N. Cheng, M. Ghasemi, P. Chen, M. Lyu, D. He, J.H. Yun, Y. Du, Y. Wang, S. Ding, A. Armin, P. Meredith, G. Liu, H.M. Cheng, L. Wang, Ligand-assisted cation-exchange engineering for high-efficiency colloidal Cs<sub>1-x</sub>FaxPbI<sub>3</sub> quantum dot solar cells with reduced phase segregation, *Nat. Energy.* 5 (2020) 79–88.  
<https://doi.org/10.1038/s41560-019-0535-7>.

- [29] T. Ameri, G. Dennler, C. Lungenschmied, C.J. Brabec, Organic tandem solar cells: A review, *Energy Environ. Sci.* 2 (2009) 347–363.  
<https://doi.org/10.1039/b817952b>.
- [30] D.A.R. Barkhouse, O. Gunawan, T. Gokmen, T.K. Todorov, D.B. Mitzi, Implications for CdTe and CIGS technologies production costs of indium and tellurium scarcity, *Prog. Photovoltaics Res. Appl.* 20 (2015) 6–11.  
<https://doi.org/10.1002/pip>.
- [31] S. Chen, J.H. Yang, X.G. Gong, A. Walsh, S.H. Wei, Intrinsic point defects and complexes in the quaternary kesterite semiconductor  $\text{Cu}_2\text{ZnSnS}_4$ , *Phys. Rev. B - Condens. Matter Mater. Phys.* 81 (2010) 35–37.  
<https://doi.org/10.1103/PhysRevB.81.245204>.
- [32] X. Liu, Y. Feng, H. Cui, F. Liu, X. Hao, G. Conibeer, D.B. Mitzi, M. Green, The current status and future prospects of kesterite solar cells: a brief review, *Prog. Photovoltaics Res. Appl.* 24 (2016) 879–898. <https://doi.org/10.1002/pip.2741>.
- [33] H. Katagiri, N. Sasaguchi, S. Hando, S. Hoshino, J. Ohashi, T. Yokota, Preparation and evaluation of  $\text{Cu}_2\text{ZnSnS}_4$  thin films by sulfurization of E-B evaporated precursors, *Sol. Energy Mater. Sol. Cells.* 49 (1997) 407–414.  
[https://doi.org/10.1016/S0927-0248\(97\)00119-0](https://doi.org/10.1016/S0927-0248(97)00119-0).
- [34] W. Shockley, H. Queisser, Detailed balance limit of efficiency of p-n junction solar cells, *Renew. Energy Four Vol. Set.* 2–4 (2018) 35–54.  
<https://doi.org/10.4324/9781315793245-44>.
- [35] H. Wang, Progress in thin film solar cells based on  $\text{Cu}_2\text{ZnSnS}_4$ , *Int. J. Photoenergy.* 2011 (2011). <https://doi.org/10.1155/2011/801292>.
- [36] S. Schorr, The crystal structure of kesterite type compounds: A neutron and X-ray diffraction study, *Sol. Energy Mater. Sol. Cells.* 95 (2011) 1482–1488.  
<https://doi.org/10.1016/j.solmat.2011.01.002>.
- [37] K. Muska, Study of Composition and Thermal Treatments of Quaternary Compounds for Monograin Layer Solar Cells, 2012.
- [38] K. Sun, F. Liu, X. Hao, Kesterite  $\text{Cu}_2\text{ZnSnS}_{4-x}\text{Se}_x$  Thin Film Solar Cells, in: *Thin Film. Photovoltaics*, IntechOpen, 2022: p. 13.  
<https://doi.org/10.5772/intechopen.101744>.
- [39] E. Mellikov, M. Altosaar, M. Kauk-Kuusik, K. Timmo, D. Meissner, M. Grossberg,

- J. Krustok, O. Volobujeva, Growth of CZTS-Based Monograins and Their Application to Membrane Solar Cells, in: K. Ito (Ed.), *Copp. Zinc Tin Sulfide-Based Thin-Film Sol. Cells*, John Wiley & Sons Ltd, Chichester, UK, 2015: pp. 289–309. <https://doi.org/10.1002/9781118437865.ch13>.
- [40] A. Fairbrother, E. García-Hemme, V. Izquierdo-Roca, X. Fontané, F.A. Pulgarín-Agudelo, O. Vigil-Galán, A. Pérez-Rodríguez, E. Saucedo, Development of a selective chemical Etch to improve the conversion efficiency of Zn-rich Cu<sub>2</sub>ZnSnS<sub>4</sub> solar cells, *J. Am. Chem. Soc.* 134 (2012) 8018–8021. <https://doi.org/10.1021/ja301373e>.
- [41] H.T. Kim, D. Kim, C. Park, Temperature effects on Cu<sub>2</sub>ZnSnS<sub>4</sub> (CZTS) films deposited by spraying method, *Mol. Cryst. Liq. Cryst.* 564 (2012) 155–161. <https://doi.org/10.1080/15421406.2012.691733>.
- [42] C.A.D. Rodriguez, G. Tremiliosi-Filho, Electrochemical Deposition, in: *Encycl. Tribol.*, Springer US, Boston, MA, 2013: pp. 918–922. [https://doi.org/10.1007/978-0-387-92897-5\\_700](https://doi.org/10.1007/978-0-387-92897-5_700).
- [43] X. Song, X. Ji, M. Li, W. Lin, X. Luo, H. Zhang, A review on development prospect of CZTS based thin film solar cells, *Int. J. Photoenergy.* 2014 (2014). <https://doi.org/10.1155/2014/613173>.
- [44] M.A. Shafi, L. Khan, S. Ullah, A. Bouich, H. Ullah, B. Mari, Synthesis of CZTS kesterite by pH adjustment in order to improve the performance of CZTS thin film for photovoltaic applications, *Superlattices Microstruct.* (2022) 107185. <https://doi.org/10.1016/j.spmi.2022.107185>.
- [45] A. V. Moholkar, S.S. Shinde, A.R. Babar, K.U. Sim, Y. bin Kwon, K.Y. Rajpure, P.S. Patil, C.H. Bhosale, J.H. Kim, Development of CZTS thin films solar cells by pulsed laser deposition: Influence of pulse repetition rate, *Sol. Energy.* 85 (2011) 1354–1363. <https://doi.org/10.1016/j.solener.2011.03.017>.
- [46] D. Depla, S. Mahieu, J.E. Greene, *Sputter Deposition Processes*, Third Edition, Elsevier Ltd., 2010. <https://doi.org/10.1016/B978-0-8155-2031-3.00005-3>.
- [47] S. Zhuk, A. Kushwaha, T.K.S. Wong, S. Masudy-Panah, A. Smirnov, G.K. Dalapati, Critical review on sputter-deposited Cu<sub>2</sub>ZnSnS<sub>4</sub> (CZTS) based thin film photovoltaic technology focusing on device architecture and absorber quality on the solar cells performance, *Sol. Energy Mater. Sol. Cells.* 171 (2017) 239–252. <https://doi.org/10.1016/j.solmat.2017.05.064>.

- [48] M. Kumar, A. Dubey, N. Adhikari, S. Venkatesan, Q. Qiao, Strategic review of secondary phases, defects and defect-complexes in kesterite CZTS-Se solar cells, *Energy Environ. Sci.* 8 (2015) 3134–3159. <https://doi.org/10.1039/c5ee02153g>.
- [49] W. Wang, G. Chen, H. Cai, B. Chen, L. Yao, M. Yang, S. Chen, Z. Huang, The effects of SnS<sub>2</sub> secondary phases on Cu<sub>2</sub>ZnSnS<sub>4</sub> solar cells: A promising mechanical exfoliation method for its removal, *J. Mater. Chem. A.* 6 (2018) 2995–3004. <https://doi.org/10.1039/c7ta08242h>.
- [50] K. Kaur, M. Sood, N. Kumar, H.H. Nazari, G.S. Gudavalli, T.P. Dhakal, M. Kumar, Critical role of Zn/Sn ratio to enhance Cu-Zn-Sn-S solar cell efficiency by suppressing detrimental Cu<sub>2</sub>-xS secondary phase, *Sol. Energy Mater. Sol. Cells.* 179 (2018) 22–30. <https://doi.org/10.1016/j.solmat.2018.02.005>.
- [51] M. Bär, B.A. Schubert, B. Marsen, S. Krause, S. Pookpanratana, T. Unold, L. Weinhardt, C. Heske, H.W. Schock, Impact of KCN etching on the chemical and electronic surface structure of Cu<sub>2</sub>ZnSnS<sub>4</sub> thin-film solar cell absorbers, *Appl. Phys. Lett.* 99 (2011). <https://doi.org/10.1063/1.3650717>.
- [52] R. Chen, J. Fan, H. Li, C. Liu, Y. Mai, Efficiency enhancement of Cu<sub>2</sub>ZnSnS<sub>4</sub> solar cells via surface treatment engineering, *R. Soc. Open Sci.* 5 (2018) 171163. <https://doi.org/10.1098/rsos.171163>.
- [53] K. Timmo, M. Altosaar, J. Raudoja, M. Grossberg, M. Danilson, O. Volobujeva, E. Mellikov, Chemical etching of Cu<sub>2</sub>ZnSn(S,Se)<sub>4</sub> monograin powder, *Conf. Rec. IEEE Photovolt. Spec. Conf.* (2010) 1982–1985. <https://doi.org/10.1109/PVSC.2010.5616411>.
- [54] H. Xie, Y. Sánchez, S. López-Marino, M. Espíndola-Rodríguez, M. Neuschitzer, D. Sylla, A. Fairbrother, V. Izquierdo-Roca, A. Pérez-Rodríguez, E. Saucedo, Impact of Sn(S,Se) secondary phases in Cu<sub>2</sub>ZnSn(S,Se)<sub>4</sub> solar cells: A chemical route for their selective removal and absorber surface passivation, *ACS Appl. Mater. Interfaces.* 6 (2014) 12744–12751. <https://doi.org/10.1021/am502609c>.
- [55] A. Weber, R. Mainz, H.W. Schock, On the Sn loss from thin films of the material system Cu-Zn-Sn-S in high vacuum, *J. Appl. Phys.* 107 (2010). <https://doi.org/10.1063/1.3273495>.
- [56] M. Kauk-Kuusik, M. Altosaar, K. Muska, M. Pilvet, J. Raudoja, K. Timmo, T. Varema, M. Grossberg, E. Mellikov, O. Volobujeva, Post-growth annealing effect

- on the performance of Cu<sub>2</sub>ZnSnSe<sub>4</sub> monograin layer solar cells, *Thin Solid Films*. 535 (2013) 18–21. <https://doi.org/10.1016/j.tsf.2012.11.075>.
- [57] J.J. Scragg, T. Ericson, T. Kubart, M. Edoff, C. Platzer-Björkman, Chemical insights into the instability of Cu<sub>2</sub>ZnSnS<sub>4</sub> films during annealing, *Chem. Mater.* 23 (2011) 4625–4633. <https://doi.org/10.1021/cm202379s>.
- [58] T. Slimani Tlemcani, F.C. El Moursli, M. Taibi, F. Hajji, E.B. Benamar, S. Colis, G. Schmerber, D. Muller, A. Slaoui, A. Dinia, M. Abd-Lefdil, One step electrodeposited CZTS thin films: Preparation and characterization, *Proc. 2014 Int. Renew. Sustain. Energy Conf. IRSEC 2014*. (2014) 89–93. <https://doi.org/10.1109/IRSEC.2014.7059867>.
- [59] I.S. Babichuk, M.O. Semenenko, S. Golovynskyi, R. Caballero, O.I. Datsenko, I. V. Babichuk, J. Li, G. Xu, R. Qiu, C. Huang, R. Hu, I. Golovynska, V. Ganus, B. Li, J. Qu, M. Leon, Control of secondary phases and disorder degree in Cu<sub>2</sub>ZnSnS<sub>4</sub> films by sulfurization at varied subatmospheric pressures, *Sol. Energy Mater. Sol. Cells*. 200 (2019). <https://doi.org/10.1016/j.solmat.2019.109915>.
- [60] O. P. Singh, N. Muhunthan, V. N. Singh, B. P. Singh, Effect Of Annealing Time On The Composition, Microstructure And Band Gap Of Copper Zinc Tin Sulfide Thin Films, *Adv. Mater. Lett.* 6 (2015) 2–7. <https://doi.org/10.5185/amlett.2015.6584>.
- [61] J. Zhong, Z. Xia, M. Luo, J. Zhao, J. Chen, L. Wang, X. Liu, D.J. Xue, Y.B. Cheng, H. Song, J. Tang, Sulfurization induced surface constitution and its correlation to the performance of solution-processed Cu<sub>2</sub>ZnSn(S,Se)<sub>4</sub> solar cells, *Sci. Rep.* 4 (2014) 1–9. <https://doi.org/10.1038/srep06288>.
- [62] E. Mellikov, D. Meissner, T. Varema, M. Altosaar, M. Kauk, O. Volobujeva, J. Raudoja, K. Timmo, M. Danilson, Monograin materials for solar cells, *Sol. Energy Mater. Sol. Cells*. 93 (2009) 65–68. <https://doi.org/10.1016/j.solmat.2008.04.018>.
- [63] M. Altosaar, A. Jagomägi, M. Kauk, M. Krunks, J. Krustok, E. Mellikov, J. Raudoja, T. Varema, Monograin layer solar cells, *Thin Solid Films*. 431–432 (2003) 466–469. [https://doi.org/10.1016/S0040-6090\(03\)00167-6](https://doi.org/10.1016/S0040-6090(03)00167-6).
- [64] C. Leiner, F.P. Wenzl, C. Sommer, G. Peharz, Improving the effectiveness of photovoltaic devices by light guiding optical foils, *Nonimaging Opt. Effic. Des.*

- Illum. Sol. Conc. XIII—Commemorating 50th Anniv. Nonimaging Opt. 9955 (2016) 995508. <https://doi.org/10.1117/12.2237866>.
- [65] C.O. Colpan, Y. Nalbant, M. Ercelik, *Fundamentals of Fuel Cell Technologies*, Compr. Energy Syst. 4–5 (2018) 1107–1130. <https://doi.org/10.1016/B978-0-12-809597-3.00446-6>.
- [66] S. Ebnesajjad, *Surface and Material Characterization Techniques*, 2014. <https://doi.org/10.1016/b978-0-323-26435-8.00004-6>.
- [67] M. Abd Mutalib, M.A. Rahman, M.H.D. Othman, A.F. Ismail, J. Jaafar, *Scanning Electron Microscopy (SEM) and Energy-Dispersive X-Ray (EDX) Spectroscopy*, Elsevier B.V., 2017. <https://doi.org/10.1016/B978-0-444-63776-5.00009-7>.
- [68] Horiba, *What is Raman Spectroscopy?*, (n.d.). <https://www.horiba.com/int/scientific/technologies/raman-imaging-and-spectroscopy/raman-spectroscopy/>.
- [69] M. Dimitrievska, A. Fairbrother, X. Fontané, T. Jawhari, V. Izquierdo-Roca, E. Saucedo, A. Pérez-Rodríguez, *Multiwavelength excitation Raman scattering study of polycrystalline kesterite Cu<sub>2</sub>ZnSnS<sub>4</sub> thin films*, Appl. Phys. Lett. 104 (2014). <https://doi.org/10.1063/1.4861593>.
- [70] U.A. Jayasooriya, R.D. Jenkins, *Introduction to Raman Spectroscopy*, in: *An Introd. to Laser Spectrosc.*, Springer US, Boston, MA, 2002: pp. 77–104. [https://doi.org/10.1007/978-1-4615-0727-7\\_3](https://doi.org/10.1007/978-1-4615-0727-7_3).
- [71] T. Markvart, L. Castañer, *Principles of Solar Cell Operation*, Elsevier Ltd, 2012. <https://doi.org/10.1016/B978-0-12-385934-1.00001-5>.
- [72] W. Ananda, *External quantum efficiency measurement of solar cell*, QiR 2017 - 2017 15th Int. Conf. Qual. Res. Int. Symp. Electr. Comput. Eng. 2017-Decem (2017) 450–456. <https://doi.org/10.1109/QIR.2017.8168528>.
- [73] O. Breitenstein, J. Bauer, M. Kittler, T. Arguirov, W. Seifert, *EBIC and luminescence studies of defects in solar cells*, Scanning. 30 (2008) 331–338. <https://doi.org/10.1002/sca.20112>.
- [74] M. Guc, S. Levchenko, I. V. Bodnar, V. Izquierdo-Roca, X. Fontane, L. V. Volkova, E. Arushanov, A. Pérez-Rodríguez, *Polarized Raman scattering study of kesterite type Cu<sub>2</sub>ZnSnS<sub>4</sub> single crystals*, Sci. Rep. 6 (2016) 1–7. <https://doi.org/10.1038/srep19414>.

- [75] A. Fairbrother, V. Izquierdo-Roca, X. Fontané, M. Ibáñez, A. Cabot, E. Saucedo, A. Pérez-Rodríguez, ZnS grain size effects on near-resonant Raman scattering: optical non-destructive grain size estimation, *CrystEngComm*. 16 (2014) 4120–4125. <https://doi.org/10.1039/C3CE42578A>.
- [76] T. Sriv, K. Kim, H. Cheong, Low-Frequency Raman Spectroscopy of Few-Layer 2H-SnS<sub>2</sub>, *Sci. Rep.* 8 (2018) 2–8. <https://doi.org/10.1038/s41598-018-28569-6>.
- [77] K. Timmo, M. Altosaar, M. Pilvet, V. Mikli, M. Grossberg, M. Danilson, T. Raadik, R. Josepson, J. Krustok, M. Kauk-Kuusik, The effect of Ag alloying of Cu<sub>2</sub>(Zn,Cd)SnS<sub>4</sub> on the monograin powder properties and solar cell performance, *J. Mater. Chem. A*. 7 (2019) 24281–24291. <https://doi.org/10.1039/c9ta07768e>.